

### 7.3.2 Kernel Plus Quantification Procedure

Fig. 7.4 outlines the procedure for detecting and quantifying an upgrade using the Kernel Plus method and the three sets of data. To start, one establishes the Kernel Plus model, which includes both AMK and self-calibration. Then, this Kernel Plus model, representing the “old” turbine, is used to make a prediction/estimation of power output under a new weather profile  $\mathbf{x}$  in either Data1 or Data2—the result is denoted as  $\hat{y}(\mathbf{x}^{(1)})$  and  $\hat{y}(\mathbf{x}^{(2)})$ , respectively. Here  $\hat{y}(\mathbf{x}^{(1)})$  and  $\hat{y}(\mathbf{x}^{(2)})$  are  $\hat{y}^{\text{KP}}(\cdot)$  but for notational simplicity and without ambiguity, the superscript, KP, is dropped. Consequently, the corresponding power output residuals can be computed. Had a turbine undergone an upgrade, one would expect the residuals before and after the upgrade to be different. A  $t$ -test is used to detect a potential difference in the residuals. Suppose that  $n_1$  and  $n_2$  are the number of data points in Data1 and Data2, respectively. The statistical test procedure is presented in Algorithm 7.3.

---

**Algorithm 7.3** Statistical test procedure for upgrade detection.

---

1. Compute the residuals before and after an upgrade. For Data1,  $\mathfrak{R}(\mathbf{x}^{(1)}) := y(\mathbf{x}^{(1)}) - \hat{y}(\mathbf{x}^{(1)})$ , and for Data2,  $\mathfrak{R}(\mathbf{x}^{(2)}) := y(\mathbf{x}^{(2)}) - \hat{y}(\mathbf{x}^{(2)})$ ;
2. Compute the two sample means and the corresponding standard deviations by using the following formula,

$$\begin{aligned}\bar{\mathfrak{R}}_k &= \frac{\sum_{j=1}^{n_k} \mathfrak{R}(\mathbf{x}_j^{(k)})}{n_k}, \quad k = 1, 2, \quad \text{and,} \\ s_k &= \sqrt{\frac{\sum_{j=1}^{n_k} (\mathfrak{R}(\mathbf{x}_j^{(k)}) - \bar{\mathfrak{R}}_k)^2}{n_k - 1}}, \quad k = 1, 2.\end{aligned}\tag{7.9}$$

3. Then, calculate the pooled estimate of standard deviation,  $\hat{\sigma}_r$ , by

$$\hat{\sigma}_r = \sqrt{\frac{(n_1 - 1)s_1^2 + (n_2 - 1)s_2^2}{n_1 + n_2 - 2}}.\tag{7.10}$$

4. The  $t$  statistic is calculated by

$$t = \frac{\bar{\mathfrak{R}}_2 - \bar{\mathfrak{R}}_1}{\hat{\sigma}_r \cdot \sqrt{\frac{1}{n_1} + \frac{1}{n_2}}}.\tag{7.11}$$

5. Finally, calculate the p-value of the  $t$  statistic. The smaller the p-value, the more significant the difference.
- 

The procedure in Algorithm 7.3 is devised to confirm any detectable difference resulting from an upgrade. The output is binary: either the upgrade

produces a statistically significant difference in a turbine's performance or it does not.

If the  $t$ -test above does indicate a significant difference, how much difference in terms of power generation does the upgrade produce? To answer this question, Lee et al. [133] define a quantifier as follows,

$$\text{DIFF}(\mathbf{x}) = \frac{\sum_{\mathbf{x} \in \mathbb{D}_{\text{test}}} (y(\mathbf{x}) - \hat{y}(\mathbf{x}))}{\sum_{\mathbf{x} \in \mathbb{D}_{\text{test}}} y(\mathbf{x})} \times 100\%, \quad (7.12)$$

where  $\mathbb{D}_{\text{test}}$  is a test dataset and can be either Data1 or Data2, so that  $\mathbf{x}$  can accordingly be either  $\mathbf{x}^{(1)}$  or  $\mathbf{x}^{(2)}$ . Similar to the residual analysis described above, comparing  $\text{DIFF}(\mathbf{x}^{(2)})$  with  $\text{DIFF}(\mathbf{x}^{(1)})$  for the test turbine, i.e.,  $\text{DIFF}^{\text{test}} = \text{DIFF}(\mathbf{x}^{(2)}) - \text{DIFF}(\mathbf{x}^{(1)})$ , produces the difference demonstrated in the test turbine before and after the upgrade. If one conducts the same analysis to the control turbine, it produces a  $\text{DIFF}^{\text{ctrl}}$ . The final quantification is the difference between the two turbines, i.e.,  $\text{DIFF} = \text{DIFF}^{\text{test}} - \text{DIFF}^{\text{ctrl}}$ .

### 7.3.3 Upgrade Detection

Using the **Turbine Upgrade Dataset** but just two weeks' worth of data for Data1 and Data2, Lee et al. [133] apply both the Kernel Plus method and the binning method to the two pairs of turbines and conduct a residual analysis. When using the binning method for upgrade quantification, one simply replaces the dashed-line rectangle in Fig. 7.4 with the binning method (the version with air density adjustment).

For an upgraded turbine, a method is supposed to produce a large  $t$ -statistic (in its absolute value), which further leads to a small p-value that signifies the difference between the residuals, whereas for a turbine without upgrade, a small  $t$  statistic, or equivalently, a large p-value is expected. The commonly used threshold of a p-value to indicate significance is 0.05, which is what Lee et al. [133] use in their analysis.

Table 7.4 presents the outcomes from the residual analysis of both pairs of turbines. The Kernel Plus method has significant outcomes consistent with the upgrade action while the binning method does not.

The outcome of the binning method is attributable to the still large amount of uncertainty unaccounted for in its residuals. To intuitively understand the outcomes of the statistical tests, Lee et al. [133] present the residual plots using data from the test turbine in the VG installation pair when applying the binning method and the Kernel Plus method, respectively. The residual plots are presented in Fig. 7.5. The residuals of the binning method exhibit an obvious pattern (leading to bias) and have a large dispersion, suggesting a poor model fit and large uncertainty, whereas the residuals of the Kernel Plus method have a considerably smaller dispersion and exhibit a random pattern, indicating an adequate model fit and reduced uncertainty.

TABLE 7.4 Comparing the Kernel Plus and binning methods on their ability to detect turbine upgrade.

Turbine	Binning		Kernel Plus		
		<i>t</i> statistic	p-value	<i>t</i> statistic	p-value
VG installation pair	Test	-0.46	0.65	2.24	0.025
	Control	-2.54	0.01	-0.14	0.89
Pitch angle adjustment pair	Test	5.09	$3.89 \times 10^{-7}$	3.18	0.002
	Control	4.51	$6.84 \times 10^{-6}$	-1.71	0.09

Source: Lee et al. [133]. With permission.

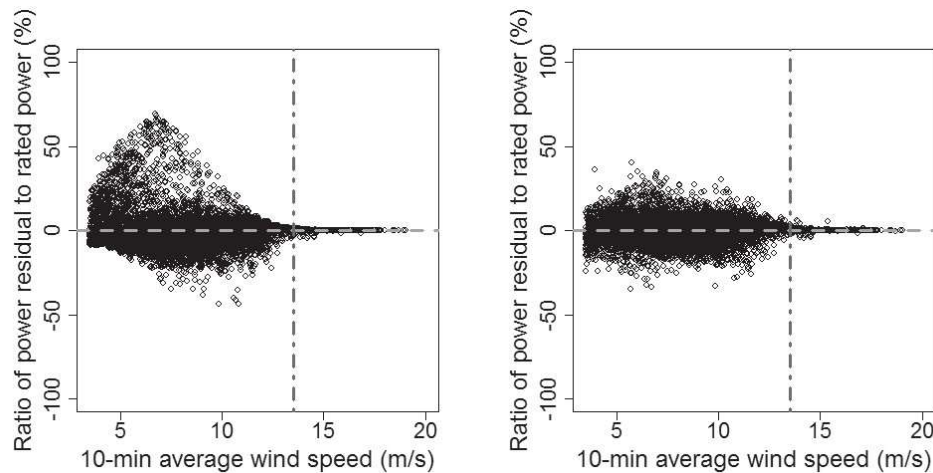


FIGURE 7.5 Residual plots. Left panel: after IEC binning is applied; right panel: after Kernel Plus is applied. The vertical dashed line indicates the rated wind speed. (Reprinted with permission from Lee et al. [133].)

TABLE 7.5 Sensitivity analysis of Kernel Plus-based turbine upgrade quantification.

$r$	2%	3%	4%	5%	6%	7%	8%	9%
$r'$	1.25%	1.87%	2.49%	3.11%	3.74%	4.36%	4.98%	5.60%
DIFF	1.97%	2.56%	3.15%	3.73%	4.30%	4.86%	5.42%	5.97%
DIFF/ $r'$	1.58	1.37	1.27	1.20	1.15	1.11	1.09	1.07

Source: Shin et al. [198]. With permission.

### 7.3.4 Upgrade Quantification

As it is done for the covariate matching in Table 7.3, let us conduct a sensitivity analysis for the Kernel Plus-based method, again using the data from the pitch angle adjustment pair. The outcome is presented in Table 7.5. One can see that the Kernel Plus method does an adequate job, but performs slightly worse than the covariate matching on this simulated case.

When applying to the VG installation pair, the DIFF value is 1.48%. Recall that the quantification from the covariate matching is UPG = 1.13%. It seems that the Kernel Plus method tends to over-estimate the upgrade effect. Please note that the DIFF values reported here are different from those reported in [133], because of the difference in data. Lee et al. [133] use two weeks' worth of data in the post-upgrade period, whereas the results above are obtained using eight weeks of data. Should the post-upgrade period be shortened to two weeks, the DIFF value is 1.81%.

To visualize a multi-dimensional response surface, like the response from the Kernel Plus method, analysts can condition some of the covariates on a constant value and average the others over all possible values. Lee et al. [133] produce a series of one-dimensional power curves under different combinations of  $\rho$  and  $I$ . Three settings each are chosen for  $\rho$  and  $I$ , respectively, which are  $\rho = (1.15, 1.18, 1.21)$  and  $I = (0.08, 0.12, 0.16)$ . Altogether, there are nine combinations. The power curves presented in Fig. 7.6 are produced based on the data from the test turbine in the VG installation pair and include those produced by using both the Kernel Plus method and the binning method.

When using the Kernel Plus method, there are observable differences in several subplots between the power curves before and after the upgrade. The difference is pronounced around the rated wind speed. By comparison, the binning method produces power curves with no visually detectable difference. This result is consistent with the message of the previous subsections.

## 7.4 AN ACADEMIA-INDUSTRY CASE STUDY

In Section 7.1, we mention that one difficulty in quantifying the benefit of a turbine upgrade is due to the lack of a good method to validate the estimated effect. Currently, it appears that a viable way to address this issue, yet still

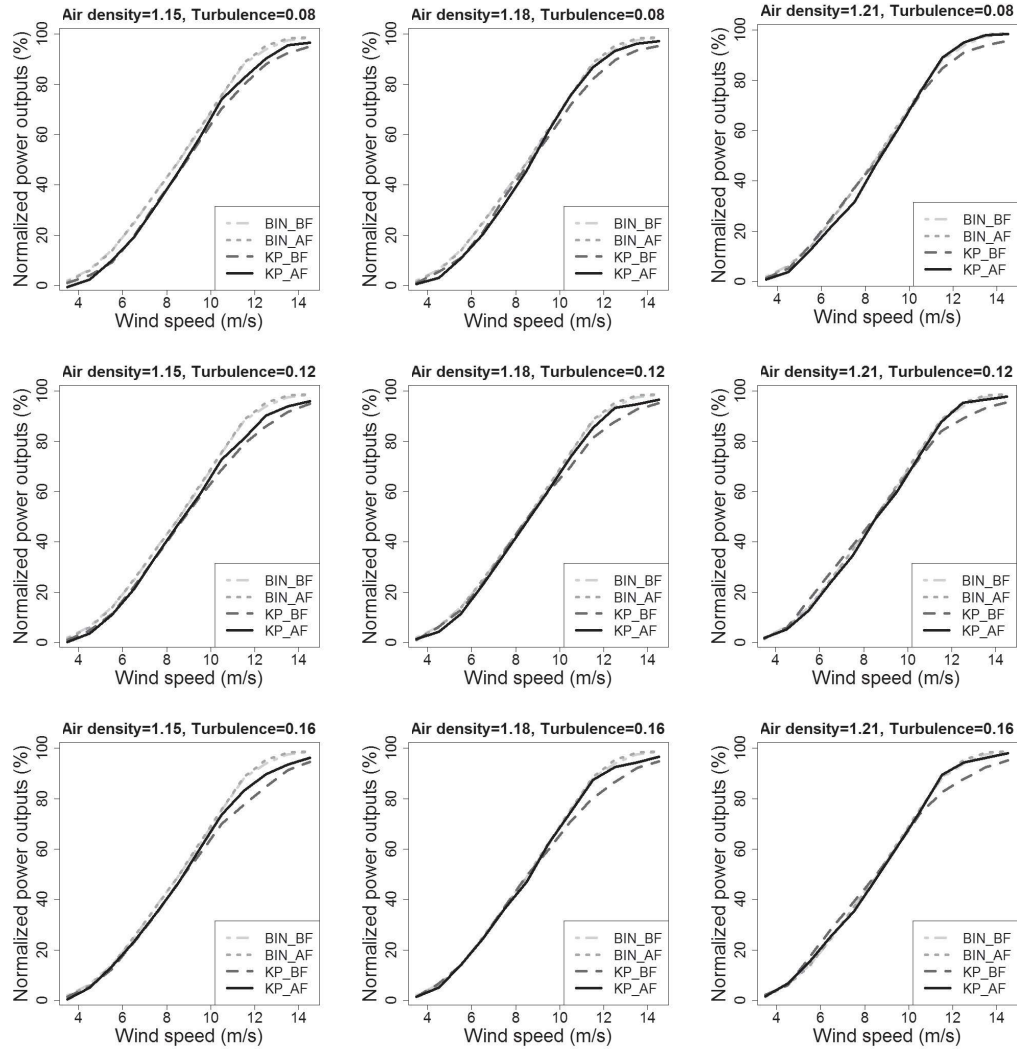


FIGURE 7.6 Power curves conditioned on air density and turbulence intensity and averaged across wind directions. BIN\_BF: binning method before upgrade; BIN\_AF: binning method after upgrade; KP\_BF: Kernel Plus method before upgrade; KP\_AF: Kernel Plus method after upgrade. (Reprinted with permission from Lee et al. [133].)

indirect, is to use two different methods to cross validate each other. Comparison between the covariate matching method and the Kernel Plus method serves that purpose.

Hwangbo et al. [95] present an academia-industry joint case study, in which an academic institution and a wind technology company use their respective method to analyze eight pairs of turbines from two wind farms, four pairs per farm. The academic institution’s method is the Kernel Plus method described in Section 7.3, whereas the company’s method uses high-frequency data via primarily a direct power comparison approach that relies less on the environmental data. The company method is referred to as the power-vs-power method.

In the next subsections, we briefly explain, based on the materials in [95], the power-vs-power method and then present the joint case study. The data used in this joint study is proprietary, and is therefore not included as one of the datasets associated with the book.

#### 7.4.1 The Power-vs-Power Method

The basic idea behind the power-vs-power approach is similar in spirit to that of the covariate matching. The difference is that the company’s specific method used in the joint study relies on the high-frequency historian data, usually a data point per a few seconds to a few data points per second. By contrast, the covariate matching in Section 7.2 and Kernel Plus in Section 7.3 both use the 10-min data. The amount of the high-frequency data could be as much as 600 times more than the 10-min data for the same time duration. The power-vs-power method uses additional mechanisms to control for the environmental influence—the controlling mechanisms are often called *filters* in industry practice.

The power-vs-power approach entails five main steps, outlined in Algorithm 7.4.

Step 1 is to ensure the validity of the assumption that when two turbines are close enough in space, it is likely that the wind and environmental conditions they are subject to are comparable. This assumption may not be reasonable for the situation when one turbine is in the wake of the other one. Step 1 is to identify the free wind sectors in the turbine operational data and then use only the free sector data in the subsequent analysis.

Step 2 performs an air density normalization. The thought behind this is similar to that of using the density-normalized wind speed, as recommended by the IEC [102]. In the case of the power-vs-power approach, no wind speed measurements are involved in the latter power comparison steps. For this reason, density normalization must be accomplished by direct normalization of the power values for the below rated region.

Step 3 is another step designed to verify and uphold the assumption that both turbines must “see” the same conditions and must operate similarly.

---

**Algorithm 7.4** Five main steps in the power-vs-power approach.

1. Determine the valid wind sectors and eliminate the wind and power measurements taken under wake conditions. Also apply all other data filters (Status.Flag, Yaw.Error, etc.).
  2. Apply a power density normalization, namely, normalize the wind power output through  $y \times \rho/\rho_0$ , where  $\rho_0$  is the sea-level dry air density. Use the density-normalized power in the subsequent analysis.
  3. If necessary, verify whether there is any other source of variation significantly affecting the power difference between the pre-upgrade and post-upgrade periods. If such a source of variation is identified, further reduce the dataset so that its effect is controlled for.
  4. Compute the bin-wise power difference, namely, calculate the power production difference of the test turbine, relative to that of the control turbine, for each of the power output bins, for both the pre-upgrade and post-upgrade periods.
  5. Compute the power difference produced by the VG installation over the whole power output spectrum.
- 

When there are obvious sources of variation, additional filters may be needed to split the data into sets of equal conditions.

After completion of the pre-processing steps that filter, clean, and normalize the data, Step 4 of the power-vs-power approach is to compute the bin-wise power difference between the two turbines. Specifically,

- Take the high-frequency power output data of the control turbine and partition the data into  $B$  bins by using a bin width of, say, 100 kW. The bin width can be adjusted for other applications, but, for megawatts capacity turbines, 100 kW appears to be a reasonable default number.
- For each bin, calculate the median of the power difference between the test turbine and the control turbine.
- Conduct the above two steps for the pre-upgrade and post-upgrade periods individually. Denote the resulting power differences by  $\Delta\bar{y}_b^{\text{PRE}}$  and  $\Delta\bar{y}_b^{\text{POST}}$ , respectively, for  $b = 1, \dots, B$ .
- Conduct a bin-wise comparison between the control and test turbine for the pre-upgrade period to verify the performance similarities between the pair of turbines.
- Calculate the bin-wise power difference as  $\Delta\bar{y}_b = \Delta\bar{y}_b^{\text{POST}} - \Delta\bar{y}_b^{\text{PRE}}$ , for  $b = 1, \dots, B$ .

Finally, Step 5 of the power-vs-power approach combines all the bin-wise power differences by using the weights derived from the power distribution over a given year; the resulting metric serves as the estimate of the upgrade effect. The detailed procedure is:

- Compute a power curve as a function of wind speed using the measurements taken from the control turbine. Alternatively, one can use the turbine manufacturer's certified reference power curve.
- Using the power curve, find the specific wind speeds,  $V_{b,\text{left}}$  and  $V_{b,\text{right}}$ , that correspond, respectively, to the lower and upper bound of the  $b$ -th power bin. Convert the wind speed distribution into a power distribution through

$$P(y_b) = F_V(V_{b,\text{right}}) - F_V(V_{b,\text{left}}),$$

where  $y_b$  is the midpoint of the  $b$ -th power bin,  $F_V(\cdot)$  is the cumulative distribution function of wind speed, and  $P(y_b)$  is the probability of the  $b$ -th power bin or, intuitively, the relative occurrence frequency of that particular power bin in the period of evaluation (i.e., a given year).

- Estimate the overall upgrade effect as

$$\Delta_{\text{upgrade}} = \frac{\sum_{b=1}^B \Delta \bar{y}_b \cdot P(y_b)}{\sum_{b=1}^B y_b \cdot P(y_b)} \times 100\%. \quad (7.13)$$

#### 7.4.2 Joint Case Study

In this case study, the upgrade action is VG installation. Four turbine pairs are taken from each of two wind farms, making a total of eight pairs. Both wind farms are inland but of different terrain complexity. The historian data is collected in high temporal resolution (about one Hertz) with no averaging applied; this is the high-frequency data referred to earlier. The 10-min data is produced from the historian data. Periods that are known to be under curtailment are manually excluded prior to the analysis.

##### Wind Farm #1

The layout of the four turbine pairs on the first wind farm is illustrated in Fig. 7.7. The wind farm is on a terrain of medium complexity. The turbines on the farm belong to the general 2 MW turbine class. The VG installation took place in a summer month of 2014, but it was conducted on different days for each of the four VG turbines. There are six months of turbine data, including wind speed and wind power, in the pre-upgrade period and 13 months of the data in the post-upgrade period. Several of the environmental measurements, such as air density and humidity, are taken from the mast. Missing data is common in all datasets and in both periods. Other details of the datasets and turbines are withheld due to the confidentiality agreement in place.

The estimated VG effect on the four pairs of turbines is presented in

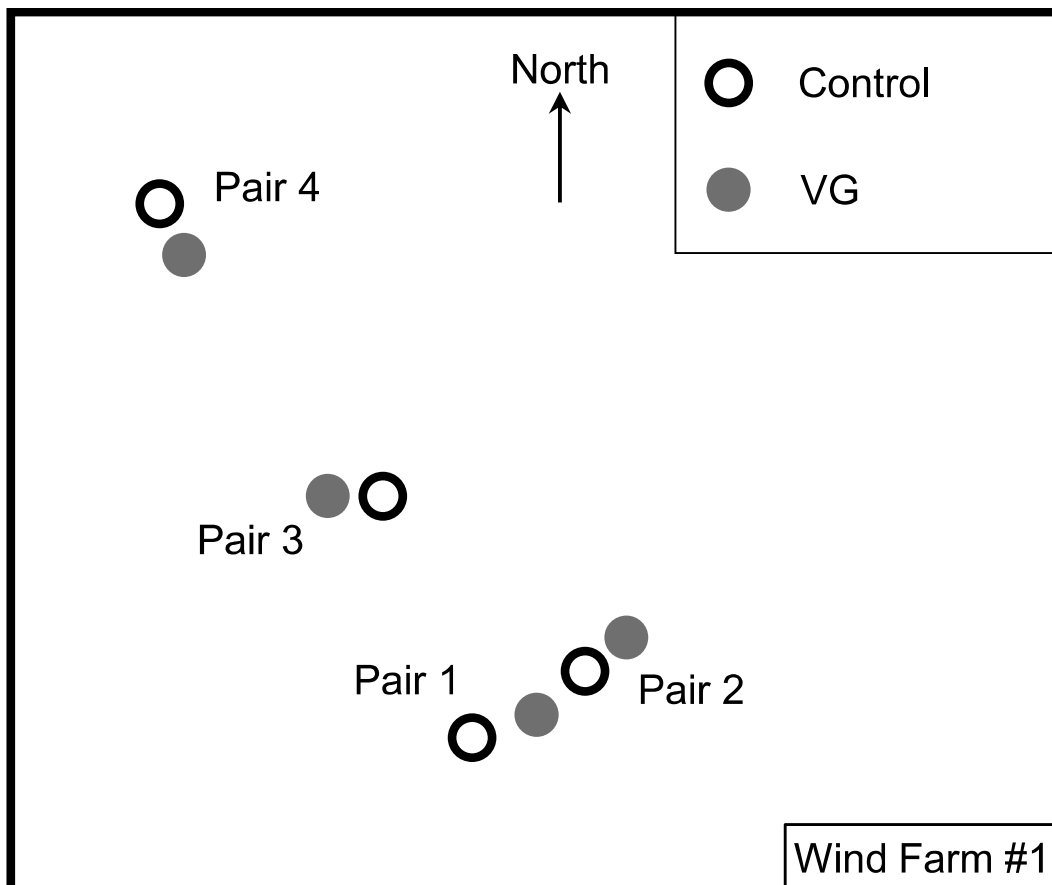


FIGURE 7.7 Layout of the four turbine pairs on wind farm #1. The distance among the turbines are not scaled precisely, but their relative positions, as well as their locations on the farm, reflect the reality. The between-turbine distances are expressed as multiples of the rotor radius,  $R$ , as follows: Pair 1,  $14R$ ; Pair 2,  $11R$ ; Pair 3,  $6R$ ; and Pair 4,  $9R$ . The met mast is directly north of all turbine pairs. Its distance to the turbine pairs are: Pair 1 & Pair 2, 11 km; Pair 3, 8.8 km; and Pair 4, 6 km. (Reprinted with permission from Hwangbo et al. [95].)

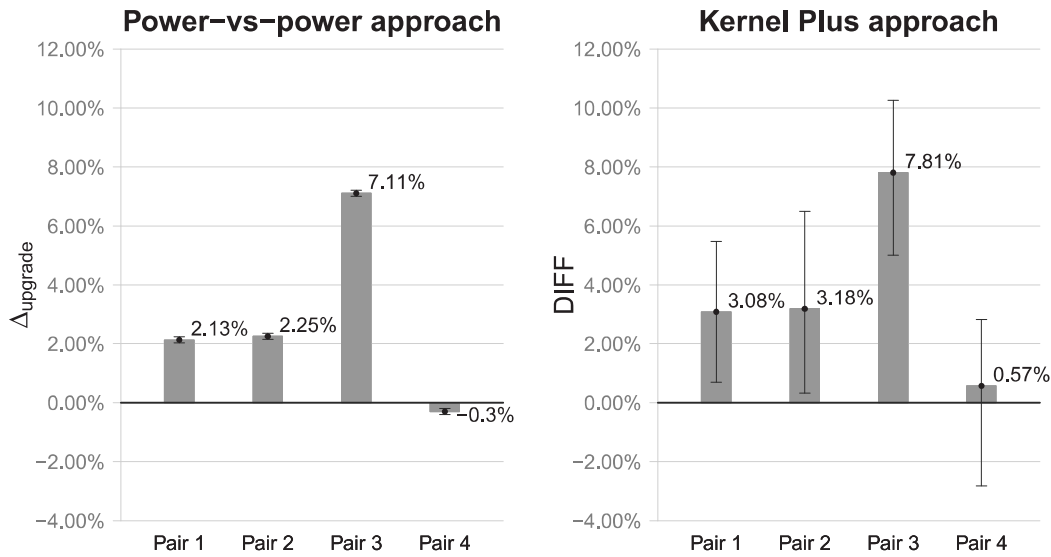


FIGURE 7.8 Estimates of the VG effect, together with the respective 90% confidence intervals, on the four pairs of turbines on wind farm #1. (Reprinted with permission from Hwangbo et al. [95].)

Fig. 7.8. Uncertainty quantification is conducted via the bootstrap resampling method, so that the 90% confidence intervals are added in the plot on top of the respective mean estimates. Understandably, the two sets of estimates are not exactly the same, but they are reasonably consistent, especially in terms of the relative significance of the VG effect on a specific turbine. The difference between the two sets of estimates are within the margin of error, and the overall difference between the two methods, averaged over the four pairs of turbines, is about 0.86%, with the Kernel Plus slightly overestimating relative to the power-vs-power approach.

## Wind Farm #2

The layout of the four turbine pairs on the second wind farm is illustrated in Fig. 7.9. The wind farm is in a coastal area and on relatively flat terrain. The turbines on the second farm belong also to the general 2 MW turbine class. The VG installation took place in December of 2015 and was also conducted on different days for each of the four VG turbines. The duration of the common period where both the turbine data and mast data are available is 3.5 months in the pre-upgrade period and one month in the post-upgrade period. In this analysis, because the mast is close to the turbines, the wind speed measurements, together with the rest of the environmental measurements, are taken from the mast. Humidity is not measured on site. The average of the humidity measurements from two nearby weather stations is thus used, one located at 10 km north of the wind farm and the other at 10 km east of the farm. Missing data is also common in all datasets and in both periods. Other

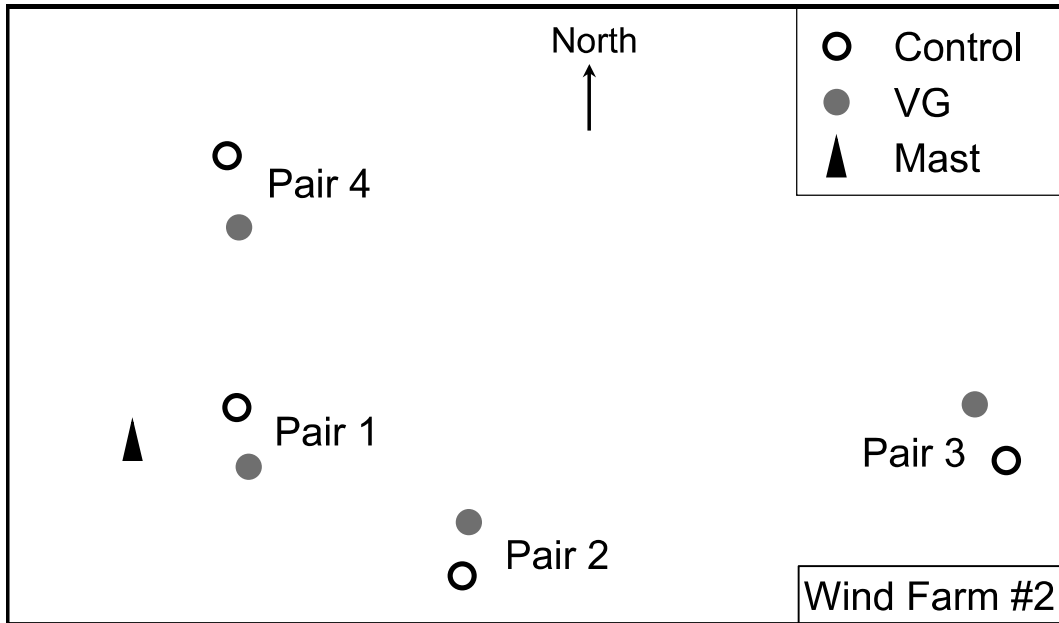


FIGURE 7.9 Layout of the four turbine pairs on wind farm #2. The between-turbine distances are: Pair 1,  $6R$ ; Pair 2,  $6.6R$ ; Pair 3,  $6.6R$ ; and Pair 4,  $7.4R$ . The met mast's distance to the turbine pairs are: Pair 1, 0.2 km, Pair 2, 1.3 km; Pair 3, 3.6 km; and Pair 4, 1.3 km. (Reprinted with permission from Hwangbo et al. [95].)

details of the datasets and turbines are withheld due to the confidentiality agreement in place.

The estimated VG effect on the four pairs of turbines is presented in Fig. 7.10. Again, one can observe consistent outcomes from the two methods: the overall difference between the two methods, averaged over the four pairs of turbines, is about 0.15%, with the Kernel Plus still slightly overestimating relative to the power-vs-power approach.

#### 7.4.3 Discussion

This academia-industry joint exercise presents a pair of upgrade quantification methods that are profoundly different in their respective underlying design and data usage. The profound difference in these two methods in fact lends more credibility in cross validation when they are employed to evaluate the same upgrade cases. The upgrade effects estimated by the two respective methods differ, on average, 0.86% and 0.15%, respectively, suggesting a good degree of consistency between them.

The power-vs-power method is simple to understand. But the data filtering procedure appears to be *ad hoc* and relies heavily on domain expertise and field judgment. By using the high-frequency data and having a larger sample

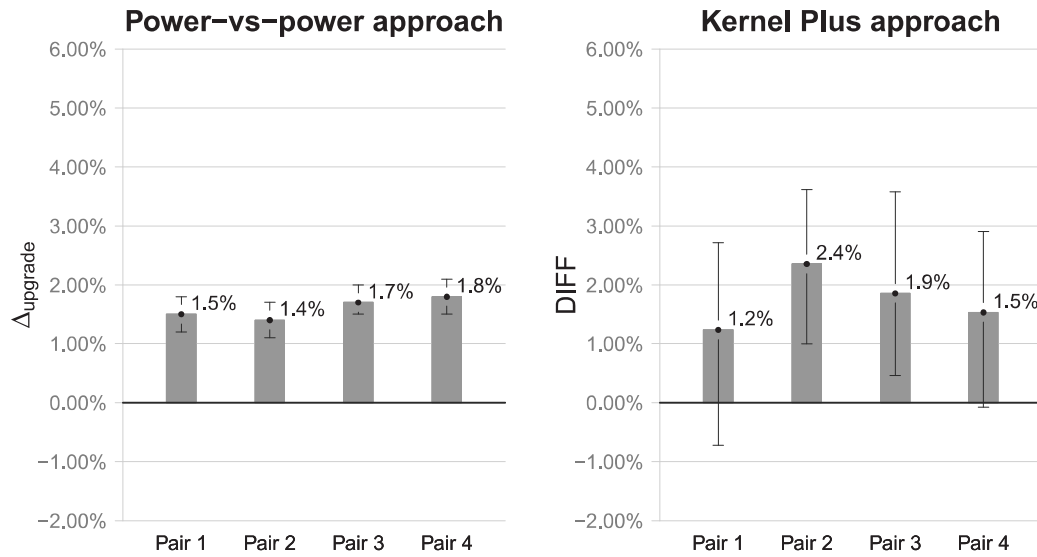


FIGURE 7.10 Estimates of the VG effects, together with the respective 90% confidence intervals, on the four pairs of turbines on wind farm #2. (Reprinted with permission from Hwangbo et al. [95].)

size, the power-vs-power approach enjoys the benefit of producing upgrade effect estimates with tighter confidence intervals.

The Kernel Plus method can possibly be applied to a single turbine when a control turbine does not exist. This explains why the Kernel Plus passed a blind test [50] in which no prior knowledge of control and VG turbines was given and no turbine pairs were provided. Yet, it is always beneficial to have a control turbine, whenever possible, as an additional reference. The premise of Kernel Plus is that it controls for the influence of the environmental factors through the learning of a multi-dimensional power curve model, but the inputs currently included in the power curve model may not be comprehensive enough. It is possible, of course, that measurements of certain important environmental factors are not available on a wind farm or analysts may not have realized yet the importance of certain other environmental factors. Improving the capability and accuracy of the underlying power curve method is always desirable.

While the general understanding of the VG effect is an extra 1–5% wind power production, it is a bit surprising to see that the quantification of Pair #3 on Farm #1 yields a greater than 7% improvement. As noted before, Wind Farm #1 is a medium complexity site that makes the wind inflow conditions complicated. Hwangbo et al. [95] believe that the VG effect tends to be greater when the wind inflow condition is more turbulent on a complex terrain. Whether this is accurate needs future studies.

It is generally a good idea to test on more than one pair of turbines and get a site average to represent the turbine upgrade effect for a specific farm.

The averaged upgrade effect from a few turbine pairs on the same farm is more stable, as the farm-level averaging irons out potential biases and reduces variability. The decision for wind farm owners/operators is not whether to install VGs on a particular turbine, but rather, whether to install VGs on the tens or even hundreds of turbines on their wind farm. For that purpose, the site-specific average is a more indicative metric. On Farm #1, the site average of VG effect is about 2.80% based on the power-vs-power approach and 3.66% based on the Kernel Plus. As for the performance on Farm #2, which is flat and at which wind inflow conditions are simpler and measured with higher confidence, the VG effects fall into a narrower range, with the site average at 1.60% based on the power-vs-power approach and at 1.75% based on the Kernel Plus method. The range of the site-averaged VG effects is consistent with what is anticipated in industrial practice.

## **7.5 COMPLEXITIES IN UPGRADE QUANTIFICATION**

To conclude this chapter, we would like to discuss a few general issues encountered in the upgrade quantification effort. Most of the issues do not have a perfect solution yet, making the continuous effort in solving the upgrade quantification problem still much appreciated.

### **Bias Correction**

One reason that the Kernel Plus uses a self-calibration procedure is to correct potential biases in upgrade effect estimation. It turns out that the bias issue is not only limited to the model-based approach like Kernel Plus. It happens also to the covariate matching approach and the power-vs-power approach. After years of research, it becomes clearer to us that whichever method can correct the bias in upgrade effect estimation outperforms the peer methods that do not do so very well.

When applying a quantification method to the control turbine data, one would ideally expect a zero upgrade effect, since the turbine undergoes no change. Apparently, this is not achieved by most of the existing methods, and because of this, a control turbine is needed as the datum to adjust the estimation of upgrade effect for the test turbine. Consider a simple case in which the data is taken from a control turbine and then duplicated and treated as the data for the test turbine. In this fashion, one in fact has two identical datasets. When an upgrade quantification method is applied to these two sets of data, it should presumably yield a zero upgrade effect. To much a surprise, many of the methods still do not. While it is easy to see the existence of the bias, how best to correct the bias eludes the analysts. The self-calibration procedure plus the control/test difference used in the Kernel Plus method provides certain degrees of safeguard.

### **Wind Speed Adjustment**

When building the Kernel Plus model or aligning the covariates in the match-

ing approach, wind speed measurements are used. The wind speed measurements may be from either a nearby mast or the nacelle. The wind measurement, if from the nacelle, is in the wake of the rotor. Installation of vortex generators alters wind flow separation behind the rotor, so much so that for the same free inflow wind in front of the rotor, the wind speed measurements taken by the nacelle anemometer before and after the VG installation are most likely different. This difference could introduce a degree of inaccuracy if left unaddressed.

IEC 61400-12-2 [104] deals with nacelle measurements through a nacelle transfer function (NTF), which is the relation between the free inflow wind speed and that measured at the nacelle anemometer. Typically an NTF can be obtained by comparing the nacelle measurements with that on a nearby mast or with a nacelle mounted LIDAR (light detection and ranging) sensor. Some operators establish an NTF for a VG turbine, so that the wind speed after the VG installation can be adjusted using the NTF. In practice, however, an NTF is rarely available, because obtaining it and continuously calibrating it are costly.

In the absence of a nacelle transfer function, Hwangbo et al. [95] introduce a wind speed adjustment procedure, acting similarly as an NTF. The shortcoming of the procedure in [95] is that the adjustment quality and accuracy is not yet verified with actual physical measurements.

Another idea to address the wind speed measurement issue is to avoid using the wind speed measured on the test turbine when building a power curve model. If wind speed measurements are available on a met mast in its physical vicinity, that would be the best. Even without a met mast nearby, analysts can consider using the wind speed measured on a neutral turbine in its vicinity, which is not affected by the VG installation as much as the wind speed measured on the test turbine.

### Annualization

When an upgrade quantification is conducted, wind farm owners or operators would like to know the benefit in terms of annual energy production. As one has seen in the examples presented earlier, there are not always a full year's worth of data available in the post-upgrade period for conducting such comparison. For the Kernel Plus method, having a full year of data in the post-upgrade period poses another problem. The post-upgrade period is known as Data2 in the Kernel Plus method, which is supposedly of the same length as that of Data1. If Data2 is one year's worth, then the total amount of data needed, combining Data0 through Data2, would have been three years' worth. This data amount requirement is too demanding. On top of that, as we see in Chapter 6, a turbine's own production efficiency characteristics may change in the span of three years even in the absence of any upgrade action, adding additional confounding effect to be shielded off in the already difficult task of estimating the upgrade benefit.

When using data from a shorter period, or a subset of data from one year

span, one may extrapolate the estimated upgrade effect to the whole year. This process is called *annualization*. The process of annualization is actually explained in Steps 4 and 5 of the power-vs-power approach. The idea is that when estimating the upgrade effect, conduct the estimation for a set of power bins. Assuming that the bin-wise upgrade effect stay more or less the same for the whole year, analysts extrapolate the estimated upgrade effect to AEP by re-weighting the bin-wise upgrade effect with the empirical distribution of wind power. For the re-weighting formula, please see Eq. 7.13.

## GLOSSARY

---

**AEP:** Annual energy production

**AMK:** Additive-multiplicative kernel method

**BIN:** Binning method

**BIN\_AF:** Binning method, after upgrade

**BIN\_BF:** Binning method, before upgrade

**DIFF:** Upgrade effect quantification when using Kernel Plus

**IEC:** International Electrotechnical Commission

**KP:** Kernel Plus

**KP\_AF:** Kernel Plus, after upgrade

**KP\_BF:** Kernel Plus, before upgrade

**LIDAR:** Light detection and ranging

**MD:** Mahalanobis distance

**NTF:** Nacelle transfer function

**pdf:** Probability density function

**SDM:** Standardized difference of means

**UPG:** Upgrade effect

**VG:** Vortex generator

## EXERCISES

---

- 7.1 Using the Turbine Upgrade Dataset, please present the boxplots of  $y^{\text{test}}$  for the pre-upgrade and post-upgrade periods, respectively. Please do this for the unmatched data and matched data and for the respective test turbine in both turbine pairs. What do you observe?

- 7.2 The current quantification outcome of the covariate matching is not annualized. To get an AEP, we need to go through the following procedure.
- Conduct the covariate matching analysis using the same parameters as used in this chapter, but compute the bin-wise upgrade effect. Use the bin width of 100 kW. Do this only for the VG installation pair.
  - Take the `Inland Wind Farm Dataset1`, which has more than one year's worth of data of four turbines from the same wind farm, and estimate the distribution of wind power output by pooling the data from the four turbines. Still use the bin width of 100 kW.
  - Use the re-weighting formula to compute the AEP effect due to the VG installation. How much is it different from the eight-week outcome?
- 7.3 Conduct the covariate matching analysis using the pitch angle adjustment pair.
- Estimate the upgrade effect by using, respectively, two weeks', five weeks', or eight weeks' worth of post-upgrade data. Observe how sensitive the method is to the length of the post-upgrade period.
  - Conduct annualization using the power distribution estimated in Exercise 7.2(b). Apply the annualization to the above three post-upgrade period choices. Are the differences in the AEPs greater than that in the upgrade effect estimation in (a)?
- 7.4 Conduct the covariate matching analysis using the pitch angle adjustment pair, but use the reverse priority order among the covariates, i.e.,  $y^{\text{ctrl}}$ ,  $I$ ,  $S$ ,  $\rho$ ,  $D$ , and  $V$ . Compute the SDMs and present them in a table similar to the lower half of Table 7.1. Does the matching procedure still significantly reduce the SDM? Go ahead and estimate the UPG again. How much is the new UPG different from what was estimated in this chapter (which is 3.16%)?
- 7.5 The current quantification outcome of the Kernel Plus is not annualized. To get an AEP, we need to go through the following procedure.
- Conduct the Kernel Plus, but compute the bin-wise upgrade effect. Again, use the bin width of 100 kW and do this only for the VG installation pair.
  - Take the power distribution estimated in Exercise 7.2(b) and use the re-weighting formula to compute the AEP of the VG installation. How much is it different from the eight-week outcome?

- 7.6 Conduct the Kernel Plus-based analysis using the pitch angle adjustment pair.
- Estimate the upgrade effect by using, respectively, two weeks', five weeks', or eight weeks' worth of post-upgrade data. Observe how sensitive the method is to the length of the post-upgrade period.
  - Conduct annualization using the power distribution estimated in Exercise 7.2(b). Apply the annualization to the above three post-upgrade period choices. Are the differences in the AEPs greater than that in the upgrade effect estimation in (a)?
- 7.7 Replace Eq. 7.8 with the Mahalanobis distance and conduct the Kernel Plus-based analysis using the pitch angle adjustment pair. What difference does it make when this distance measure is changed? What if you use a simple Euclidean distance (unweighted)?
- 7.8 Use the binning method to replace the dashed-line rectangular box in Fig. 7.4 and treat that as a binning-based quantification method. Apply the binning-based quantification method to the two pairs of turbines and estimate the respective upgrade effect. How much are they different from the covariate matching and Kernel Plus?
- 7.9 Conduct the sensitivity analysis for the binning-based quantification, as it is done in Tables 7.3 and 7.5. Compare your results with those in Tables 7.3 and 7.5.
- 7.10 Take the control turbine data from the pitch angle adjustment pair, duplicate the data and treat it as if it were the test turbine data. Now, you have two identical datasets.
- Multiply the test turbine power by  $r$  (for all power values), for  $r = 0, 1, 2, 3, 4$ , and 5%.
  - For each  $r$ , employ, respectively, the covariate matching, Kernel Plus, and binning methods to estimate the upgrade effect. Tabulate the outcomes similar to the presentation in Table 7.3.
  - For each original power value in the test turbine set (before being multiplied by an  $r$  in (a)), multiply it by a random number, drawn uniformly from the range [0, 5%]. Compute the effective power increase rate for the test turbine power data. Employ, respectively, the covariate matching, Kernel Plus, and binning methods to estimate the upgrade effect. Compare the estimated upgrade effect and the effective power increase rate.



Taylor & Francis  
Taylor & Francis Group  
<http://taylorandfrancis.com>

# Wake Effect Analysis

---

While a wind turbine is operating, the rotating blades disturb the natural flow of wind and create turbulence for the downstream turbines. During this process, the turbine absorbs kinetic energy in wind and converts the energy into electricity. As a result, the wind loses some of its original kinetic energy after the rotor, exhibiting reduction in its speed. Such a phenomenon differentiating the after-rotor wind flow from the free-stream one (before the rotor) is referred to as wake effect.

Understanding and quantifying the wake effect plays an important role in improving wind turbine designs and operations as well as wind farm layout planning. Being a physical phenomenon, the majority of the wake effect models are understandably physics based. Modelers resort in particular to sophisticated, computational fluid dynamics (CFD) models that can achieve a higher accuracy [129]. However, using the CFD models entails significant computational challenges. For example, running a large eddy simulation, one of the popular CFD methods, requires days or even weeks of computation on supercomputers for analyzing a single-wake situation [192]. The abundance of wind farm operational data motivates the development of data science methods for analyzing and estimating wake effect, which is the focus of this chapter.

## 8.1 CHARACTERISTICS OF WAKE EFFECT

---

The wake of a turbine propagates with a certain range of angles, and its impact remains effective up to a certain distance from the turbine. Fig. 8.1 illustrates a snapshot of a single-wake situation. A single wake refers to the circumstance in which two operating turbines are involved and one is in the wake of the other for a given wind direction. In the figure,  $\theta$  denotes an acute angle between the wind direction and the line connecting the two turbines. For the wind direction shown in Fig. 8.1, left panel, the wind passes through Turbine 1 along the center line. The wake caused by Turbine 1 affects the downstream region with a range of angles (the shaded area). The wind speed loss due to the wake is greater for locations closer to the upstream turbine

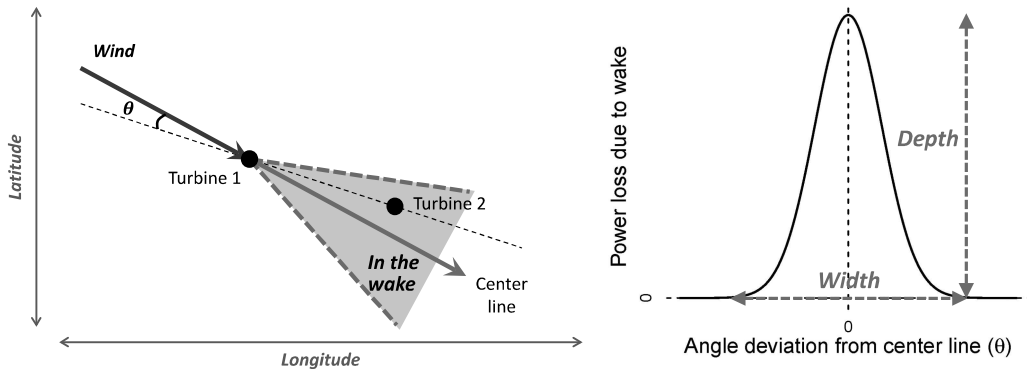


**FIGURE 8.1** Characteristics of wind turbine wake effect. Left panel: wake region and  $\theta$ ; right panel: wake depth and wake width. (Reprinted with permission from Hwangbo et al. [98].)

(Turbine 1) and closer to the center line. Turbine 2, its position fixed, is subject to the greatest power loss when  $\theta = 0$ . The power loss amount decreases as  $\theta$  deviates from zero. After  $\theta$  exceeds a certain value, Turbine 2 is no longer in the wake of Turbine 1. The maximum power loss when  $\theta = 0$  is referred to as the *wake depth*, whereas the range of  $\theta$  for which a turbine is in the wake of another turbine (with positive power losses) is referred to as the *wake width*. Wake depth and width are expected to remain constant when the relative positions between two turbines are fixed.

Fig. 8.2 illustrates power output of a wind turbine when it is wake free versus when it is in the wake of another turbine.

Knowledge of wake characteristics is crucial for improving power generation performance on wind farms. As wake width and depth strongly depend on the relative positions of turbines, characterizing the turbine specific wake effect facilitates the layout planning [56, 128], particularly when using the same turbine model in future wind projects. Understanding the wake characteristics also supports effective operational control of wind turbines through pitch and yaw controls [70, 146]. The pitch control can regulate the magnitude of wind speed loss in a downstream region by adjusting the energy absorption level of an upstream turbine. The yaw control can change the amount of the wind speed loss by tilting the downstream wake region. By carefully controlling the yaw of Turbine 1, Turbine 2 may be as nearly wake free as possible for a given wind direction.

## 8.2 JENSEN'S MODEL

As mentioned earlier in this chapter, sophisticated CFD wake models take long computational time to run and their use is less practical for commercial wind farm operation. A widely used, physics-based model is Jensen's model [108], due to its simplicity and easiness to compute. Jensen's model is derived by

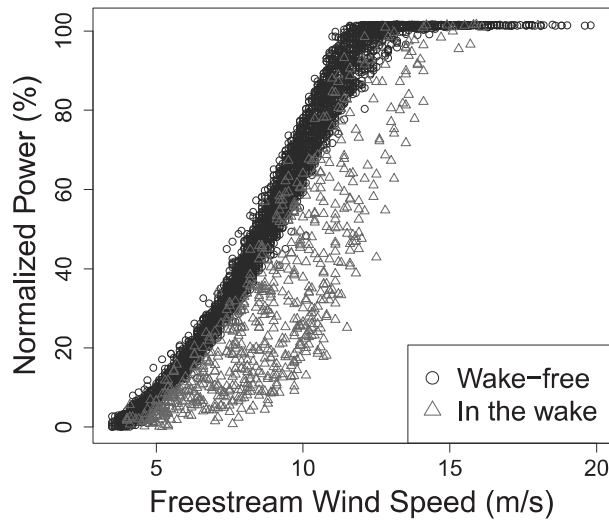


FIGURE 8.2 Power output in the wake versus that under a free-stream condition. (Reprinted with permission from Hwangbo et al. [98].)

solving an equation based on the balance of momentum. The resulting wake effect, in terms of wind speed, is expressed as

$$V_{\text{wake}} = \left\{ 1 - \frac{2}{3} \left( \frac{R}{R + \kappa \cdot d} \right)^2 \right\} \cdot V, \quad (8.1)$$

where  $R$  is the rotor radius of a wind turbine,  $d$  is the down-wind distance from the rotor, and  $\kappa$  is known as the entrainment constant. For wake effect, the entrainment constant,  $\kappa$ , is approximately 0.1. Based on Eq. 8.1, the wind speed immediately after the rotor where  $d = 0$ , is one-third of the free-stream wind speed. On the other hand, the wind speed at the down-wind distance of ten rotor diameters, i.e.,  $d = 20R$ , is about 0.926 $V$ . This is part of the reason that analysts deem  $20R$  a safe boundary beyond which the wake effect by and large weans off.

Eq. 8.1 can be simplified to  $V_{\text{wake}} = (1 - \kappa_{\text{deficit}}) \cdot V$  [232, Eq. 23], where  $\kappa_{\text{deficit}}$  depends generally on the down-wind distance. Some analysts further simplify  $\kappa_{\text{deficit}}$  to be a constant of 0.075, which, according to Eq. 8.1, corresponds roughly to  $d = 20R$ .

Apparently, Jensen's model does not directly estimate the power loss. In fact, nearly all other physics-based wake effect models do not do so, either. Instead, they primarily focus on estimating the reduced wind speed due to wake. To quantify wake power loss, these models then require an additional layer of converting the wind speed estimates into a corresponding power output—a conversion can be done by using a simple power curve model such as the IEC binning method or more complicated power curve models as presented in Chapter 5. Data science methods, on the other hand, can connect the wind

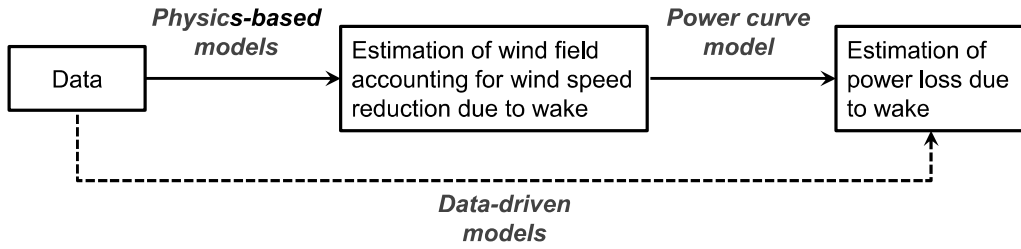


FIGURE 8.3 Wake power loss estimation procedures. (Reprinted with permission from Hwangbo et al. [98].)

speed data directly to the power output in a single step; see Fig. 8.3. In the case study section, the data-driven models are compared with the two-step approach that has Jensen's model as its first step.

### 8.3 A DATA BINNING APPROACH

---

The binning approach is rather popular in industrial practice, acting as a robust, nonparametric method, easy to understand and easy to use. Not surprisingly, it is used for estimating the wake characteristics as well. A common data binning approach for wake effect estimation is presented in Algorithm 8.1.

---

#### **Algorithm 8.1** Data binning approach.

---

1. Gather the power output data from two turbines.
  2. Choose a specific range of wind speed where the maximum power loss is expected, e.g.,  $8.0 \pm 0.5$  m/s [14], or extend the coverage of wind speed to a wider range, e.g., 5.0–11.0 m/s [146] or even to the whole wind spectrum, which is the choice used in Section 8.6.1.
  3. Plot the power difference between the two turbines under the above-specified wind speeds against the wind direction (0 degree means due north)
  4. To smooth out the noise, apply the action of binning, namely, partition the wind direction by a bin width, say  $5^\circ$ , and then average all the power difference data in a specific bin. Use the bin-wise averages as the representative of the original data.
- 

In Fig. 8.4, the dark dots constitute a scatter plot of the power differences against wind direction. Once applying the data binning approach to the raw power differences, it produces the solid line passing through the data cloud. The solid line is the estimated wake effect. The wake depth can be read from

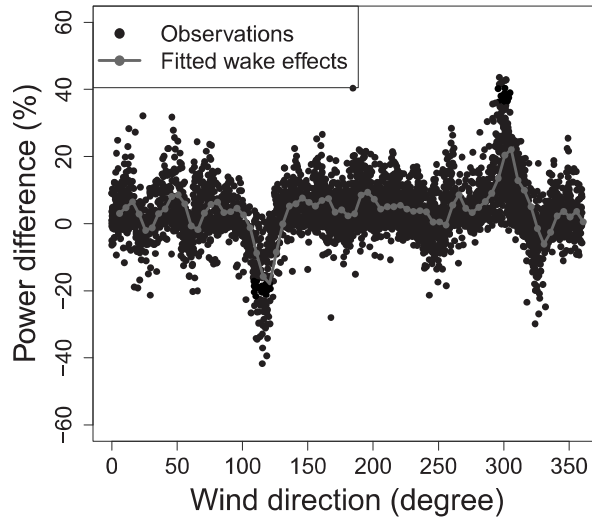


FIGURE 8.4 Data binning approach for estimating the wake effect between a pair of turbines. The between-turbine distance is four times the rotor diameter. The distance from this pair to other turbines is more than  $20R$ . (Reprinted with permission from Hwangbo et al. [98].)

the plot by observing the two peaks around  $120^\circ$  and  $300^\circ$ , respectively. As one moves along the wind direction from  $0^\circ$  to  $360^\circ$ , the roles of the two turbines, i.e., which one is wake free and which one is in the wake, are reversed. That is why one observes that one of the peaks is downward. In Fig. 8.4, the wake width is not immediately obvious. Analysts usually impose a large enough angle coverage, say,  $\theta \in (-25^\circ, 25^\circ)$ , and then verify with the estimated curve if the angle range is broad enough to represent the wake width [146]. To refine the estimation, analysts sometimes find a wind direction value on each side of the center line at which the power loss estimate is within a certain level, for example,  $\pm 5\%$  of the free-stream power, and use the angle coverage formed by these wind direction values as the estimate of wake width [14]. When using this data binning approach, the power difference from the wake-free turbine to the in-the-wake turbine, which estimates wake power loss, is not guaranteed to be positive. As a matter of fact, previous studies [169, 215] often show that some of the bin-wise estimates of the power difference is negative even after  $\theta$  moves beyond the obvious wake width region—this phenomenon is indeed evident in Fig. 8.4.

#### 8.4 SPLINE-BASED SINGLE-WAKE MODEL

Hwangbo et al. [98] develop a wake effect model based on splines. Their model is intended to estimate wake effect characteristics, such as wake width and wake depth, under single-wake situations arising between two turbines

of which modeling assumptions are easier to justify. To facilitate a successful transition from physics-based models to data-driven modeling, Hwangbo et al. incorporate certain physical understandings and considerations as constraints in the model fitting process. Because of this, the resulting single-wake model is a physics-constrained, rather than a purely, data-driven model.

#### 8.4.1 Baseline Power Production Model

Hwangbo et al. [98] start with the production economics model in Eq. 6.5 but make some changes to it. Recall that Eq. 6.5 reads as,

$$y(V) = Q(V) - u(V) + \varepsilon, \quad (8.2)$$

where  $Q(\cdot)$  is the production frontier function and  $u(\cdot)$  is the systematic inefficiency term. Eq. 6.5 is expressed as a univariate function of wind speed,  $V$ .

The baseline power production model used for wake effect modeling reads as,

$$y_t(\mathbf{x}) = Q_t(\mathbf{x}) - \eta_t(\mathbf{x}) - \omega_t(\mathbf{x}) + \varepsilon_t, \quad t = 1, \dots, N, \quad (8.3)$$

where  $t$  is the turbine index and  $N$  is the number of turbines. In the above model, the inefficiency term,  $u(\cdot)$ , is split into two terms— $\eta_t(\cdot)$  and  $\omega_t(\cdot)$ —such that  $\eta_t(\cdot)$  represents a turbine's inherent inefficiency independent of wake, whereas  $\omega_t(\cdot)$  represents the turbine's power loss due to wake. Also, the input variable is now a vector rather than wind speed only. Furthermore, Hwangbo et al. [98] postulate that both power loss terms in the above model are non-negative, i.e.,  $\eta_t(\cdot) \geq 0$  and  $\omega_t(\cdot) \geq 0$ ,  $\forall t = 1, \dots, N$ , to be consistent with the physical understanding of the phenomenon.

We said in Chapter 6 that estimating  $Q_t(\cdot)$  under a multivariate setting while satisfying the S-shape constraint is not trivial. Luckily, for the single-wake situation,  $Q_t(\cdot)$  does not have to be estimated explicitly. For a pair of turbines, one can pool together the two turbines' power production data and estimate a common production frontier. As it will become clear in the next section, Hwangbo et al. [98] establish a power difference model, which takes the *power difference* between a pair of turbines, and in doing so, the common frontier function cancels each other in the resulting model. This is to say, the production frontier function,  $Q_t(\cdot)$ , does not appear in the final wake effect model.

#### 8.4.2 Power Difference Model for Two Turbines

For a single-wake situation with two turbines, two angle variables,  $\theta_1$  and  $\theta_2$ , are used and associated, respectively, with the two turbines. Specifically,  $\theta_1$  is related to the wind direction causing power loss on Turbine 1 and  $\theta_2$  is with the wind direction under which Turbine 2 endures power loss. As illustrated in Fig. 8.5, the wind directions associated with  $\theta_1$  and  $\theta_2$  can take any value

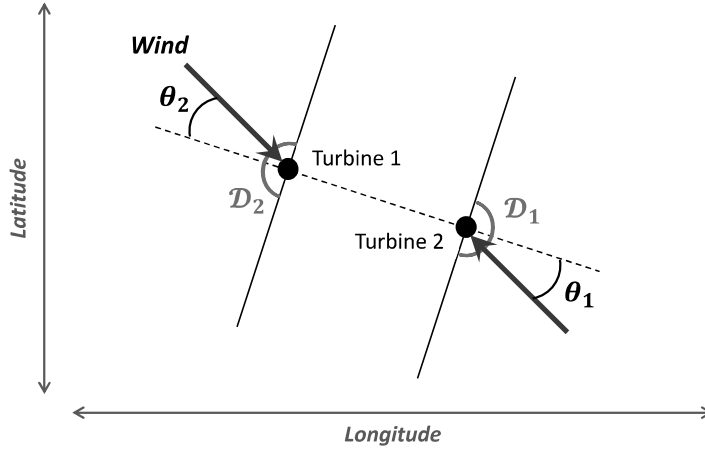


FIGURE 8.5 Notations of wind direction in wake analysis. The union of  $\mathcal{D}_1$  and  $\mathcal{D}_2$  covers the entire  $360^\circ$  wind direction. (Reprinted with permission from Hwangbo et al. [98].)

in the sets,  $\mathcal{D}_1$  and  $\mathcal{D}_2$ , respectively, given the definition of these sets stated below. For the purpose of analyzing the wake effect,  $\theta_1$  and  $\theta_2$  only need to vary in the  $180^\circ$  outer hemisphere surrounding their respective turbine. Note that  $\theta_1$  is actually on the side of Turbine 2, whereas  $\theta_2$  is on the side of Turbine 1. If one positions the zero degree of  $\theta_1$  and  $\theta_2$  at the line connecting the two turbines, then  $\theta_1, \theta_2 \in (-90^\circ, 90^\circ)$ . Denote by  $\mathcal{D}_1$  the set of wind directions corresponding to the support of  $\theta_1$ , and likewise, by  $\mathcal{D}_2$  the set of directions in which  $\theta_2$  is defined.

With this notation, applying the baseline power production model in Eq. 8.3 individually to the two turbines yields

$$\begin{aligned} y_1(\mathbf{x}) &= Q(\mathbf{x}) - \eta_1(\mathbf{x}) - \omega_1(\mathbf{x}) \cdot \mathbb{1}_{\mathcal{D}_1}(\mathbf{x}) + \varepsilon_1, \\ y_2(\mathbf{x}) &= Q(\mathbf{x}) - \eta_2(\mathbf{x}) - \omega_2(\mathbf{x}) \cdot \mathbb{1}_{\mathcal{D}_2}(\mathbf{x}) + \varepsilon_2, \end{aligned} \quad (8.4)$$

where  $\mathbb{1}_{\mathcal{D}_t}(\mathbf{x})$  is an indicator function taking the values of one, if the wind direction belongs to  $\mathcal{D}_t$ , or zero otherwise. Here, the production frontier function,  $Q(\mathbf{x})$ , is assumed to be common to the same type of turbines, and for this reason, it does not use a turbine-differentiating subscript. Taking the difference between the two equations in Eq. 8.4 leads to

$$\tilde{y}_{1-2}(\mathbf{x}) = \tilde{\eta}_{2-1}(\mathbf{x}) - \omega_1(\mathbf{x}) \cdot \mathbb{1}_{\mathcal{D}_1}(\mathbf{x}) + \omega_2(\mathbf{x}) \cdot \mathbb{1}_{\mathcal{D}_2}(\mathbf{x}) + \tilde{\varepsilon}, \quad (8.5)$$

where the tilde indicates a turbine difference term and the subscripts 1-2 and 2-1 signify the specific order of the difference. The above model is interpreted as follows: the power difference of Turbine 1 over Turbine 2 is due to the inherent production difference between the two turbines,  $\tilde{\eta}_{2-1}(\cdot)$ , and the power loss caused by the wake effect, characterized by either  $\omega_1(\cdot)$  or  $\omega_2(\cdot)$ , both depend-

ing on specific wind conditions. Because the sets,  $\mathcal{D}_1$  and  $\mathcal{D}_2$ , are mutually exclusive,  $\omega_1(\cdot)$  and  $\omega_2(\cdot)$  do not appear at the same time.

It is well known that the dominating input factors for wind power production are wind speed,  $V$ , and wind direction,  $D$ . The analysis in Chapter 5 shows that environmental factors other than wind speed and direction, such as air density, turbulence, and humidity, may also have an impact on wind power output. One advantage of using the power difference model in Eq. 8.5 is that one no longer needs to consider other environmental factors because once the power difference is taken of the two turbines, the impact of the environmental factors other than that of the wind is neutralized. Still, to be consistent with the IEC standard procedure and to further neutralize the effect of air density, Hwangbo et al. [98] decided to use the normalized wind speed, following the air density correction formula in Eq. 5.3.

For the turbine difference term and the indicator function terms in Eq. 8.5, either wind speed or wind direction, but not both, is needed as an input. The input to the indicator function  $\mathbb{1}_{\mathcal{D}_1}(\cdot)$  or  $\mathbb{1}_{\mathcal{D}_2}(\cdot)$  is wind direction. The turbine difference term,  $\tilde{\eta}_{2-1}(\cdot)$ , represents the between-turbine production difference independent of wake. Hwangbo et al. [98] thereby assume that it is only a function of wind speed, not of wind direction, as the portion of the power difference,  $\tilde{y}_{1-2}$  or  $\tilde{y}_{2-1}$ , related to wind direction should be included in the wake related term  $\omega$ .

As such, the power difference model can be expressed as:

$$\tilde{y}_{1-2}(V, D) = \tilde{\eta}_{2-1}(V) - \omega_1(V, D) \cdot \mathbb{1}_{\mathcal{D}_1}(D) + \omega_2(V, D) \cdot \mathbb{1}_{\mathcal{D}_2}(D) + \tilde{\varepsilon}, \quad (8.6)$$

where  $\tilde{\varepsilon}$  is still an i.i.d. noise, assumed to follow a normal distribution.

### 8.4.3 Spline Model with Non-negativity Constraint

In order to empirically estimate the power difference model in Eq. 8.6, Hwangbo et al. [98] assume the following model structure for the three functional terms: (a)  $\tilde{\eta}$  is modeled by a univariate cubic smoothing spline and (b) the two wake power loss terms,  $\omega_1$  and  $\omega_2$ , are modeled by bivariate thin plate splines [228], a multidimensional generalization of the smoothing splines. Recall that when Eq. 8.3 is presented, non-negativity constraints are imposed on the power loss terms, which state that  $\eta(\cdot) \geq 0$  and  $\omega(\cdot) \geq 0$ . After taking the power difference, the turbine difference term,  $\tilde{\eta}_{2-1}(\cdot)$ , no longer needs to be non-negative; in fact, it can be positive, zero, or negative. But the wake power loss terms,  $\omega_1$  and  $\omega_2$ , are still supposed to be non-negative. As such, the power difference model in Eq. 8.6 becomes a spline model with the non-negativity constraint imposed on  $\omega_1$  and  $\omega_2$ . The resulting model is referred to as the thin plate regression spline model with non-negativity (TPRS-N).

To estimate the spline-based power difference model, Hwangbo et al. [98] follow the generalized additive model (GAM) scheme [87]. GAMs represent a univariate response as an additive sum of multiple smooth functions, each having its own predictor variables. Estimation of GAMs can be performed

by implementing the backfitting algorithm for which each smooth function is fitted for the residuals of all the others, iteratively one at a time until the fitted functions converge.

The learning formulas for smoothing spline and thin plate splines follow the regularized learning formulation in Eq. 5.20. Because of the use of the iterative backfitting algorithm,  $y$  is replaced by the residual variable  $r$  in that formulation. When the algorithm starts, the residual  $r$  is the same as  $y$  (differing by the average of  $y$ ). When the algorithm proceeds, the residual from the preceding steps is used in the learning formulation, instead of the original  $y$ .

Consider  $n$  data pairs for which a residual  $r$  is paired with  $\mathbf{x}$ , i.e.,  $(\mathbf{x}_i, r_i)$  for  $i = 1, \dots, n$ . The formula for the smoothing spline can be found in Eq. 5.22 in which  $y_i$  is replaced by  $r_i$ . For thin plate splines with two predictors,  $x_1$  and  $x_2$ , the first part of the loss function is the same as in the smoothing spline, but the penalty function reads as

$$\text{Penalty}(g) = \int \int_{\mathbb{R}^2} \left[ \left( \frac{\partial^2 g(\mathbf{x})}{\partial x_1^2} \right)^2 + 2 \left( \frac{\partial^2 g(\mathbf{x})}{\partial x_1 \partial x_2} \right)^2 + \left( \frac{\partial^2 g(\mathbf{x})}{\partial x_2^2} \right)^2 \right] dx_1 dx_2. \quad (8.7)$$

For the smoothing splines, let us express the corresponding  $g(x)$  as (recall Exercise 5.4)

$$g(x) = \sum_{j=1}^n h_j(x) \beta_j, \quad (8.8)$$

where  $h_j(x)$  is the  $j^{th}$  basis function of a natural cubic spline and  $\beta_j$  is the corresponding coefficient. Then, Eq. 5.22 can be expressed as

$$\underset{\boldsymbol{\beta}}{\operatorname{argmin}} (\mathbf{r} - \mathbf{H}\boldsymbol{\beta})^T (\mathbf{r} - \mathbf{H}\boldsymbol{\beta}) + \gamma \boldsymbol{\beta}^T \boldsymbol{\Omega}_h \boldsymbol{\beta}, \quad (8.9)$$

where  $\mathbf{H}$  is a matrix whose  $(i, j)^{th}$  element is  $h_j(x_i)$  and  $\boldsymbol{\Omega}_h$  is a matrix derived from  $h(\cdot)$  (therefore the subscript) whose  $(j, k)^{th}$  element is  $\int h_j''(t) h_k''(t) dt$ . The solution is

$$\hat{\boldsymbol{\beta}} = (\mathbf{H}^T \mathbf{H} + \gamma \boldsymbol{\Omega}_h)^{-1} \mathbf{H}^T \mathbf{r}. \quad (8.10)$$

Different from the smoothing splines, the  $g(\mathbf{x})$  of the thin plate splines is expressed as

$$g(\mathbf{x}) = \mathbf{X}\boldsymbol{\beta}^{(\text{tp})} + \sum_{i=1}^n \delta_i \phi(\|\mathbf{x} - \mathbf{x}_i\|),$$

where the  $n \times 3$  matrix  $\mathbf{X} = [\mathbf{1}_n; \mathbf{x}_1; \mathbf{x}_2]$  includes the unit vector of size  $n$  as its first column and the  $n$  observations for the two covariates as its second and third columns, and  $\phi(\|\mathbf{x} - \mathbf{x}_i\|)$  is a radial basis function. Here the radial basis function is involved because analysts find that thin plate splines have a natural representation in terms of radial basis functions [228]. The three-dimensional vector  $\boldsymbol{\beta}^{(\text{tp})}$  and the  $n$ -dimensional vector  $\boldsymbol{\delta} = (\delta_1, \dots, \delta_n)^T$  are, respectively, the coefficients associated with  $\mathbf{X}$  and those associated with the

radial basis functions, and both sets of coefficients need to be estimated. The superscript “tp” is added to  $\beta$  to differentiate this vector in the thin plate splines from that in the smoothing splines.

Using the thin plate spline’s  $g(\mathbf{x})$  and its penalty function (as in Eq. 8.7) in a regularized learning formulation, like in Eq. 5.22, leads to the estimation of the model coefficients in the thin plate spline. It turns out (details skipped) that the solution is equivalent to solving

$$\min \|\mathbf{r} - \mathbf{X}\beta^{(tp)} - \Phi\delta\|^2 + \gamma\delta^T\Phi\delta, \quad \text{subject to } \mathbf{X}^T\delta = \mathbf{0}, \quad (8.11)$$

where  $\Phi$  is the radial basis matrix, defined by  $\Phi_{ji} = \phi(\|\mathbf{x}_j - \mathbf{x}_i\|) = \|\mathbf{x}_j - \mathbf{x}_i\|^2 \log \|\mathbf{x}_j - \mathbf{x}_i\|$  for  $i, j = 1, \dots, n$ .

Different from the univariate spline problem that can be solved by  $O(n)$  operations, the computations for the thin plate splines require  $O(n^3)$  operations [87]. To overcome the computational problem, Wood [228] proposes the thin plate regression splines (TPRS), which uses only  $k$  eigenbasis functions ( $k \ll n$ ) corresponding to the largest  $k$  eigenvalues of the basis matrix  $\Phi$ . Doing so reduces the rank of the basis matrix significantly.

TPRS can be fitted as follows. First, applying the eigen decomposition of  $\Phi$  leads to  $\Phi = \mathbf{U}\Lambda\mathbf{U}^T$  where  $\Lambda$  is a diagonal matrix whose diagonal elements are the eigenvalues of  $\Phi$  and arranged in a non-increasing order, i.e.,  $\Lambda_{i,i} \geq \Lambda_{i+1,i+1}$  for  $i = 1, \dots, n-1$ . Matrix  $\mathbf{U}$  is an orthogonal matrix whose columns are the eigenvectors ordered accordingly. Then, TPRS considers the first  $k$  columns of  $\mathbf{U}$ , denoted by  $\mathbf{U}_k$ , and uses them to construct a rank  $k$  eigenbasis matrix  $\Phi_k = \mathbf{U}_k\Lambda_k\mathbf{U}_k^T$ , where  $\Lambda_k$  is a  $k \times k$  diagonal matrix taking the first  $k$  rows and columns of  $\Lambda$ .

By restricting  $\delta$  in the column space of  $\mathbf{U}_k$ , i.e., let  $\delta = \mathbf{U}_k\delta_k$ , Eq. 8.11 becomes

$$\min \|\mathbf{r} - \mathbf{X}\beta^{(tp)} - \mathbf{U}_k\Lambda_k\delta_k\|^2 + \gamma\delta_k^T\Lambda_k\delta_k \quad \text{subject to } \mathbf{X}^T\mathbf{U}_k\delta_k = \mathbf{0}.$$

In expressing the above equation, one needs  $\mathbf{U}_k^T\mathbf{U}_k = \mathbf{I}$ , which is true, due to the fact that columns in  $\mathbf{U}_k$  are orthogonal by construction.

The constrained problem can be replaced by an unconstrained problem through the QR decomposition of  $\mathbf{U}_k^T\mathbf{X}$ . Specifically, form a  $\mathbf{Z}_k$  that takes the last  $k-3$  columns of the orthogonal factor of the decomposition. Restricting  $\delta_k$  to the column space of  $\mathbf{Z}_k$  by letting  $\delta_k = \mathbf{Z}_k\tilde{\delta}$  renders the constraint satisfied. Then, the rank- $k$  approximation can be used to fit TPRS by solving

$$\min \|\mathbf{r} - \mathbf{X}\beta^{(tp)} - \mathbf{U}_k\Lambda_k\mathbf{Z}_k\tilde{\delta}\|^2 + \gamma\tilde{\delta}^T\mathbf{Z}_k^T\Lambda_k\mathbf{Z}_k\tilde{\delta}, \quad (8.12)$$

for the unknown  $\beta^{(tp)}$  and  $\tilde{\delta}$ . The prediction for any given  $\mathbf{x}$  can be achieved by calculating  $\hat{\delta} = \mathbf{U}_k\mathbf{Z}_k\tilde{\delta}$  and plugging  $\hat{\delta}$  and  $\hat{\beta}^{(tp)}$  into

$$\hat{g}(\mathbf{x}) = \mathbf{X}\hat{\beta}^{(tp)} + \sum_{i=1}^n \hat{\delta}_i \phi(\|\mathbf{x} - \mathbf{x}_i\|). \quad (8.13)$$

Recall that the wake power loss term,  $\omega_t$ , is assumed non-negative to be consistent with the physical understanding of the wake effect, but the modeling procedure of TPRS does not guarantee non-negativity. In order to make sure the wake power loss is indeed non-negative, Hwangbo et al. [98] apply an exponential transformation on top of the conventional TPRS estimation in Eq. 8.13, i.e., let

$$\hat{\omega}(\mathbf{x}) = \exp \left\{ \mathbf{X} \hat{\boldsymbol{\beta}}^{(\text{tp})} + \sum_{i=1}^n \hat{\delta}_i \phi(\|\mathbf{x} - \mathbf{x}_i\|) \right\}. \quad (8.14)$$

Because of this change, instead of solving Eq. 8.12, one now aims at solving

$$\min \left\| \mathbf{r} - \exp \left\{ \mathbf{X} \boldsymbol{\beta}^{(\text{tp})} + \mathbf{U}_k \boldsymbol{\Lambda}_k \mathbf{Z}_k \tilde{\boldsymbol{\delta}}_k \right\} \right\|^2 + \gamma \tilde{\boldsymbol{\delta}}_k^T \mathbf{Z}_k^T \boldsymbol{\Lambda}_k \mathbf{Z}_k \tilde{\boldsymbol{\delta}}_k, \quad (8.15)$$

with respect to  $\boldsymbol{\beta}^{(\text{tp})}$  and  $\tilde{\boldsymbol{\delta}}_k$ .

When estimating a GAM, a constant term generally precedes the functional terms, and is estimated by using the global mean. In other words, the global mean is calculated and subtracted from the response in advance, before implementing the backfitting algorithm that estimates the rest of the functional terms. In the power difference model in Eq. 8.6, this constant term should be part of the turbine-difference term,  $\tilde{\eta}(\cdot)$ , meaning that a portion of the turbine difference is constant regardless of the wind conditions, while the other portion may change with the wind speed. For the implementation of the backfitting algorithm, Eq. 8.6 is re-expressed as

$$\tilde{y} = \alpha + [\tilde{\eta}(V) - \alpha] - \omega_1(V, D) \cdot \mathbb{1}_{D_1}(D) + \omega_2(V, D) \cdot \mathbb{1}_{D_2}(D) + \tilde{\varepsilon}. \quad (8.16)$$

One proceeds to estimate  $\alpha$  using the global mean and estimate  $[\tilde{\eta}(V) - \alpha]$  using a cubic smoothing spline (and the wake loss terms using TPRS-N). Once all the functional terms are estimated,  $\tilde{\eta}(V)$  is restored by  $\hat{\alpha} + \hat{\eta}(V)$  where  $\hat{\eta}(V)$  is the estimate of  $[\tilde{\eta}(V) - \alpha]$ .

Before implementing the backfitting algorithm, some tuning parameters need to be set, including the smoothing parameter  $\gamma$  and the value of the reduced rank  $k$  used for improving the computational efficiency of TPRS-N. There are in fact three  $\gamma$  parameters, one each for the three smooth function estimations, associated, respectively, with  $\tilde{\eta}(\cdot)$  and  $\omega(\cdot)$ 's. They are chosen based on a 10-fold cross validation while applying grid search. For the reduced rank  $k$ , Wood [228] states that the choice of  $k$  is not so critical as long as it is larger than the degrees of freedom required for the estimation. Hwangbo et al. [98] set  $k = 30$  which turns out to be large enough for the wake effect analysis application. Finally, Hwangbo et al. set a threshold,  $\epsilon_0 = 0.1$ , which determines the convergence of the model fitting. The choice of 0.1 is believed to be sufficiently small considering the magnitude of the functional estimates changing exponentially due to the imposition of non-negativity.

The backfitting algorithm for the power difference model is summarized in Algorithm 8.2.

---

**Algorithm 8.2** Backfitting algorithm for wake power loss estimation.

---

```

1: Initialize:
    $m \leftarrow 0; \hat{\alpha} \leftarrow \sum_{i=1}^n y_i/n; \hat{\eta}^m \leftarrow \mathbf{0}; \hat{\omega}_1^m \leftarrow \mathbf{0}; \hat{\omega}_2^m \leftarrow \mathbf{0}$ 
2: repeat
3:   Set  $m \leftarrow m + 1$ .
4:   Estimation of  $\hat{\eta}$ 
5:     Calculate partial residuals:  $\mathbf{r}_\eta \leftarrow \mathbf{y} - \hat{\alpha} + \hat{\omega}_1^{m-1} - \hat{\omega}_2^{m-1}$ .
6:     Set  $\hat{\eta}^m$  by fitting smoothing spline to  $\mathbf{r}_\eta$  with respect to  $\mathbf{V}$ .
7:   Estimation of  $\hat{\omega}_1$ 
8:     Calculate partial residuals:  $\mathbf{r}_{\omega_1} \leftarrow -(\mathbf{y} - \hat{\alpha} - \hat{\eta}^m - \hat{\omega}_2^{m-1})$ .
9:     Set  $\hat{\omega}_1^m$  by fitting thin plate regression spline with non-negativity
      to  $\mathbf{r}_{\omega_1}$  with respect to  $\mathbf{V}$  and  $\mathbf{D}$  for the data whose  $D \in \mathcal{D}_1$ .
10:  Estimation of  $\hat{\omega}_2$ 
11:    Calculate partial residuals:  $\mathbf{r}_{\omega_2} \leftarrow \mathbf{y} - \hat{\alpha} - \hat{\eta}^m + \hat{\omega}_1^m$ .
12:    Set  $\hat{\omega}_2^m$  by fitting thin plate regression spline with non-negativity
      to  $\mathbf{r}_{\omega_2}$  with respect to  $\mathbf{V}$  and  $\mathbf{D}$  for the data whose  $D \in \mathcal{D}_2$ .
13:  Computation of convergence criterion
14:  
$$\Delta \leftarrow \frac{||\hat{\eta}^m - \hat{\eta}^{m-1}|| + ||\hat{\omega}_1^m - \hat{\omega}_1^{m-1}|| + ||\hat{\omega}_2^m - \hat{\omega}_2^{m-1}||}{||\hat{\eta}^{m-1}|| + ||\hat{\omega}_1^{m-1}|| + ||\hat{\omega}_2^{m-1}||}.$$

15: until  $\Delta \leq \epsilon_0$  where  $\epsilon_0$  is a prescribed threshold.

```

---

## 8.5 GAUSSIAN MARKOV RANDOM FIELD MODEL

---

The spline-based wake model in the preceding section is a single-wake model. You et al. [232] present a Gaussian Markov random field (GMRF) model that makes use of the spatial correlations among multiple turbines located close to one another and estimates simultaneously the heterogeneous power outputs from multiple turbines and the wake interactions. Apparently, this GMRF model is capable of modeling circumstances involving more than single wakes.

You et al. [232] do not directly model the wake loss, but model the power output with both a global term and a local term. The global term characterizes the average power production behavior of the turbines on a farm, as a function of environmental covariates,  $\mathbf{x}$ , similar to the power curve models presented in Chapter 5, whereas the local term characterizes the turbine-to-turbine variability unique to that specific turbine location and its neighboring turbines. The global term is not exactly the same as the power curve model. The difference is that the global term uses the same coefficient vector,  $\beta$ , for all turbines on a farm, whereas the power curve model in Chapter 5 is supposed to be turbine specific; see also Exercise 8.2.

The GMRF model could be used to estimate the wake power loss *indirectly* by taking the difference of the maximum fitted value among all turbines and the power output fitted to a specific turbine. Please note that the GMRF

model does not impose the constraint that the wake power loss should be non-negative.

The GMRF model takes the model structure as

$$y_t = G(\mathbf{x}, \boldsymbol{\beta}) + L(\mathbf{x}, \boldsymbol{\zeta}_t) + \varepsilon_t, \quad t = 1, \dots, N, \quad (8.17)$$

where  $G(\cdot, \cdot)$  and  $L(\cdot, \cdot)$  are the global and local terms, referred to, respectively, in the preceding paragraph. Consider  $q$  input variables in  $\mathbf{x} = (x_1, \dots, x_q)^T$ . You et al. [232] model  $G(\cdot, \cdot)$  as an additive model of  $q$  terms, each of which is a set of univariate B-spline functions taking one of the input variables in  $\mathbf{x}$  as its input. Specifically, You et al. express

$$G(\mathbf{x}, \boldsymbol{\beta}) = G_1(x_1, \boldsymbol{\beta}^{(1)}) + \dots + G_j(x_j, \boldsymbol{\beta}^{(j)}) + \dots + G_q(x_q, \boldsymbol{\beta}^{(q)}), \quad (8.18)$$

where  $G_j(x_j, \boldsymbol{\beta}^{(j)})$  is further written as

$$G_j(x_j, \boldsymbol{\beta}^{(j)}) = \sum_{k=1}^{K^{(j)}} \beta_k^{(j)} g_k^{(j)}(x_j),$$

and the superscript,  $(j)$ , is used to indicate that the B-spline basis functions are for the  $j$ -th input variable  $x_j$ ,  $K^{(j)}$  is the number of the basis functions,  $g_k^{(j)}(\cdot)$  is the  $k$ -th univariate, global-term B-spline basis, as a function of  $x_j$ , and  $\beta_k^{(j)}$  is the  $k$ -th spline regression coefficient.

The local term is likewise modeled as

$$L(\mathbf{x}, \boldsymbol{\zeta}_t) = L_1(x_1, \boldsymbol{\zeta}_t^{(1)}) + \dots + L_j(x_j, \boldsymbol{\zeta}_t^{(j)}) + \dots + L_q(x_q, \boldsymbol{\zeta}_t^{(q)}), \quad (8.19)$$

where  $L_j(x_j, \boldsymbol{\zeta}_t^{(j)})$  is further expressed as

$$L_j(x_j, \boldsymbol{\zeta}_t^{(j)}) = \sum_{k=1}^{K^{(j)}} \zeta_{t,k}^{(j)} l_k^{(j)}(x_j),$$

and  $l_k^{(j)}(\cdot)$  is the  $k$ -th univariate, local-term B-spline basis, and  $\zeta_{t,k}^{(j)}$  is the  $k$ -th spline regression coefficient but specific to turbine  $t$ .

You et al. [232] treat  $\boldsymbol{\zeta}_t^{(j)}$  as a random effect term and model it using GMRF. To reduce the modeling complexity, they further decompose  $\boldsymbol{\zeta}_t^{(j)}$  into

$$\boldsymbol{\zeta}_t^{(j)} = \eta_t^{(j)} \boldsymbol{\zeta}^{(j)},$$

where the scalar term,  $\eta_t^{(j)}$ , captures the variations among individual turbines, while the vector term,  $\boldsymbol{\zeta}^{(j)}$ , becomes turbine-independent. With this decomposition,  $\zeta_{t,k}^{(j)}$  in Eq. 8.19 can be expressed as  $\zeta_{t,k}^{(j)} = \eta_t^{(j)} \cdot \zeta_k^{(j)}$ . The scalar random effect term,  $\eta_t^{(j)}$ , is modeled by

$$\eta_t^{(j)} | \{\eta_{t'}^{(j)} : t' \in \mathfrak{N}_t\} \sim \mathcal{N} \left( \sum_{t' \in \mathfrak{N}_t} c_{t,t'} \eta_{t'}^{(j)}, \tau_j^2 \right), \quad (8.20)$$

where  $\mathfrak{N}_t$  denotes the neighborhood of turbine  $t$ ,  $c_{t,t'}$  captures interdependence between turbines  $t$  and  $t'$ , and  $\tau_j^2$  is the variance for this conditional normal distribution, associated with the  $j$ -th input variable. Following the approach proposed in [115], You et al. [232] use the directional spatial dependence intensity to model  $c_{t,t'}$  as

$$c_{t,t'} = \alpha_1 \sin^2(\theta_{t,t'}) \left( \frac{1}{d_{t,t'}} \right)^h + \alpha_2 \cos^2(\theta_{t,t'}) \left( \frac{1}{d_{t,t'}} \right)^h, \quad (8.21)$$

where  $d_{t,t'}$  is the distance between the two turbines in question,  $\theta_{t,t'}$  is the angle between the wind direction and the line connecting turbine  $t$  and turbine  $t'$ ,  $\alpha_1$  and  $\alpha_2$  are the coefficients to be estimated by data, and  $h$  is a shape parameter, set to 0.5 by You et al. in their applications.

While implementing the method for wind applications, You et al. [232] include two primary inputs, wind speed and turbulence intensity. The global term in their GMRF model uses a B-spline function with degree 2 or higher for the wind speed input and a B-spline function of degree 1 or 2 for the turbulence intensity input. The local term uses B-spline functions of degree equaling to or smaller than their counterparts in the global term. In defining the knots for wind speeds, You et al. set five equal-distaned knots between 5 m/s and 17.5 m/s, resulting in four internal knots, respectively, at 7.5 m/s, 10 m/s, 12.5 m/s, and 15 m/s. In defining the knots for turbulence intensity, You et al. set two internal knots, with equal distance, in the turbulence intensity data range observed in their dataset. The turbulence intensity data range is [0.2, 1.5], which yields two knots at 0.63 and 1.07, respectively.

The GMRF also needs to define a neighborhood,  $\mathfrak{N}_t$ , for each turbine  $t$ . You et al. [232] primarily use the first-order neighborhood turbines, which are defined as the eight nearest turbines surrounding turbine  $t$ .

You et al. [232] estimate the model parameters through a Bayesian hierarchical inference framework that is numerically solved by a Markov chain Monte Carlo (MCMC) sampling procedure. We will discuss MCMC more in Chapter 10.

## 8.6 CASE STUDY

---

### 8.6.1 Performance Comparison of Wake Models

In this section, a few wake models are compared in terms of their prediction performance of the power difference. Because directly measuring the actual wake power loss is difficult, the prediction or estimation of the power difference becomes an important proxy alluding to a model's capability of accounting for the wake effect in wind power production. Furthermore, power difference prediction could be in and by itself useful in a number of wind energy applications—for instance, the turbine upgrade quantification discussed in Chapter 7.

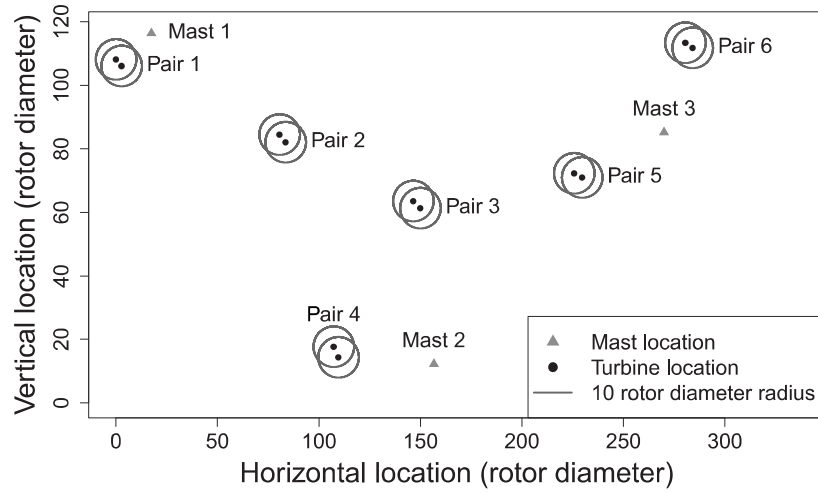


FIGURE 8.6 Locations of the six pairs of wind turbines and three met masts. The distances along both axes are expressed as a multiple of the rotor diameter of the turbines. All turbines have the same rotor diameter. (Reprinted with permission from Hwangbo et al. [98].)

TABLE 8.1 Between-turbine distances and relative positions of the six pairs of turbines. Bearing 1 to 2 indicates a relative direction of Turbine 1 to the location of Turbine 2, and Bearing 2 to 1 is similarly defined.

	Pair 1	Pair 2	Pair 3	Pair 4	Pair 5	Pair 6
Between-turbine distance	$6.8R$	$7.6R$	$8.4R$	$8.2R$	$8.2R$	$7.8R$
Bearing 1 to 2 ( $^{\circ}$ )	307.1	308.7	302.6	325.0	288.3	294.2
Bearing 2 to 1 ( $^{\circ}$ )	127.1	128.7	122.6	145.0	108.3	114.2

Source: Hwangbo et al. [98]. With permission.

This study uses the Wake Effect Dataset. Fig. 8.6 shows the relative locations of the six pairs of turbines and three met masts. The circle around each turbine is the  $20R$  radius from, or the ten times rotor diameter centering at, the turbine. All turbine pairs happen to have the northwestern-to-southeastern orientation. Hwangbo et al. [98] designate, for all turbine pairs, the turbine on the northwestern side as Turbine 1 and the one on the southeastern side as Turbine 2.

Table 8.1 provides the between-turbine distances, in terms of a multiple of the rotor radius, and the relative positional angles between a pair of turbines. Based on the specific relative positions between a pair of turbines and the notations illustrated in Fig. 8.5, one can divide wind direction into two distinct sectors of  $\mathcal{D}_1$  and  $\mathcal{D}_2$  for each turbine pair. For a wind direction  $D \in \mathcal{D}_2$ , Turbine 1 is wake free and Turbine 2 is in the wake, whereas for  $D \in \mathcal{D}_1$ , Turbine 2 is wake free and Turbine 1 is in the wake.

TABLE 8.2 Comparison of prediction error in terms of RMSE. The value in the table is the power difference relative to the maximum power of the turbine. The boldface values are the smallest in each column.

	RMSE					
	Pair 1	Pair 2	Pair 3	Pair 4	Pair 5	Pair 6
Jensen's model	0.1103	0.0887	0.1109	0.0971	0.0956	0.1020
GMRF	0.0846	0.0752	0.0888	0.0797	0.0798	0.0877
Binning	0.0778	0.0667	0.0818	0.0800	0.0706	0.0751
TPRS-N	<b>0.0668</b>	<b>0.0627</b>	<b>0.0802</b>	<b>0.0758</b>	<b>0.0683</b>	<b>0.0699</b>

Source: Hwangbo et al. [98]. With permission.

TABLE 8.3 Comparison of prediction error in terms of MAE. The value in the table is the power difference relative to the maximum power of the turbine. The boldface values are the smallest in each column.

	MAE					
	Pair 1	Pair 2	Pair 3	Pair 4	Pair 5	Pair 6
Jensen's model	0.0544	0.0530	0.0673	0.0570	0.0631	0.0565
GMRF	0.0484	0.0469	0.0568	<b>0.0470</b>	0.0497	0.0544
Binning	0.0434	0.0435	0.0532	0.0504	0.0489	0.0457
TPRS-N	<b>0.0375</b>	<b>0.0408</b>	<b>0.0523</b>	0.0477	<b>0.0447</b>	<b>0.0434</b>

Source: Hwangbo et al. [98]. With permission.

Hwangbo et al. [98] evaluate the performance of a model with respect to its out-of-sample prediction errors. For this, each turbine pair's annual data are split into training and test subsets by a ratio of 80:20. In other words, 80% of a given dataset are randomly selected to train the model and the remaining 20% are used to calculate the prediction error. To measure the prediction error, Hwangbo et al. use both RMSE and MAE.

This section presents a performance comparison of four methods: Jensen's model, the data binning approach, the GMRF model, and the TPRS-N wake model, all under the single-wake situations.

Tables 8.2 and 8.3, respectively, present the RMSE and MAE values for the four methods and six turbine pairs. Relative to the Jensen's model, three data-driven methods significantly reduce the level of uncertainty by accounting for the variation observed in the data.

Recall that GMRF is not specifically developed for the single-wake situation. By construction, GMRF is designed to perform well with more turbines since it benefits from the spatial modeling of multiple turbines at different locations. Understandably, the method loses some of the benefits when being applied to a single pair of turbines. Still, the method shows significant improvement with, on average, an 18% reduction in RMSE and 14% in MAE as compared to Jensen's model.

The data binning approach, while fitting the trend of data without any restriction, in fact attains competitive prediction errors. This should not come

as a surprise, as the binning approach is nonparametric and can adapt to local data features, as long as one uses a small enough binning resolution and there are dense enough data points to fit the binning model. The data binning approach is competitive in terms of out-of-sample prediction when compared with GMRF. The fact that its RMSE and MAE are larger than those of the TPRS-N model suggests, however, that the data binning approach overfits the (training) data. Another shortcoming of the data binning approach is that it is less insightful at providing wake characteristics.

The TPRS-N wake model, having incorporated physical constraints on wake power losses, demonstrates its superiority over other alternatives in terms of the prediction error of the power difference. It yields the smallest RMSE values across all six turbine pairs and the smallest MAE values for five among the six pairs. Its RMSE (MAE) is, on average, 30% (24%) smaller than that of Jensen's model, 15% (12%) smaller than GMRF, and 6% (7%) smaller than the data binning approach.

### 8.6.2 Analysis of Turbine Wake Effect

This section presents a study that quantifies annual wake power loss in actual wind turbine operations. Quantification of the wake power loss based on an annual period supports economic assessment of wake effect in terms of AEP. Doing so also provides practical insights into the economic impact of decisions and actions attempting to alleviate the wake power loss.

Fig. 8.7 illustrates the estimated wake characteristics using the **Wake Effect Dataset**. The wake loss is supposed to be strictly positive. What is shown in the plot is actually  $-\hat{\omega}_1(V, D) \cdot \mathbb{1}_{\mathcal{D}_1}(D) + \hat{\omega}_2(V, D) \cdot \mathbb{1}_{\mathcal{D}_2}(D)$ , so that one sees both positive and negative portions. The raw power differences of some pairs of turbines, when plotted against wind direction, exhibit large variation with several peaks and troughs. Even under such a noisy circumstance, the TPRS-N wake model captures the wake power loss signals well, by focusing on where the wake power loss is expected. In the figure, the vertical dashed lines indicate the bearings, i.e.,  $\theta_1 = 0$  or  $\theta_2 = 0$ .

Comparing Fig 8.7, bottom-left panel, to Fig. 8.4 (both generated from Pair 5), it is obvious that the TPRS-N wake loss estimation method captures the signals much better than the data binning approach could, making the subsequent derivation of the wake characteristics more convincing. One may also observe from Fig. 8.7 that the wind direction associated with the highest power loss is not exactly aligned with the bearings of the turbine pairs. This implies that there are measurement errors in wind direction. When applying the data binning approach, analysts typically generate angle bins starting from a bearing by making it the midpoint of an angle bin (and propagate with a resolution of 5 degrees, for example) and then regard the wake loss estimate of this specific bin as the wake depth. It turns out that, in the presence of measurements errors in wind direction, such a practice has an obvious disadvantage and will likely underestimate the wake depth due to the

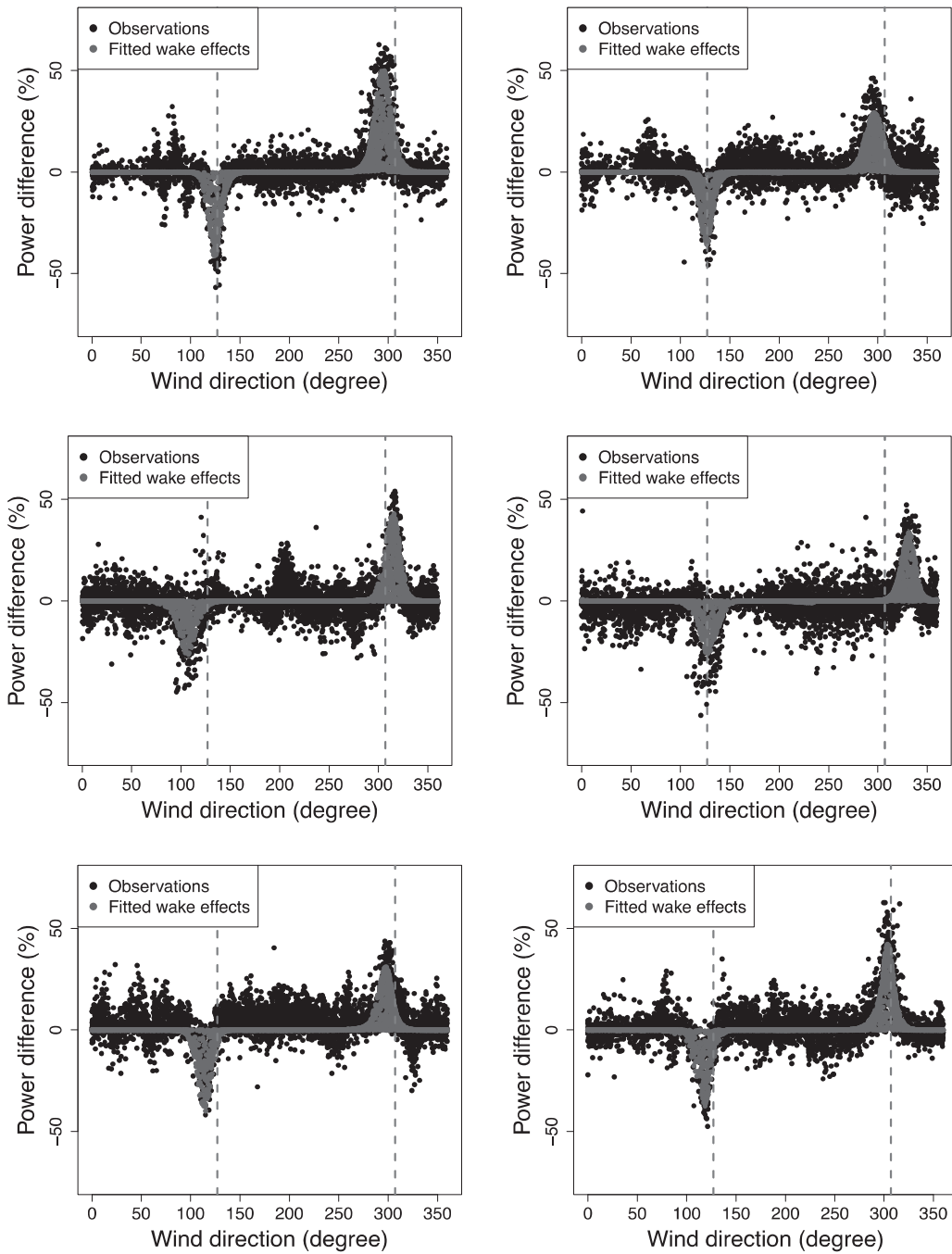


FIGURE 8.7 Estimates of the wake effect using the TPRS-N model. From top-left to bottom-right are, respectively, the estimation for Pair 1 through Pair 6. The shaded areas represent the fitted wake loss in terms of  $-\hat{\omega}_1(V, D) \cdot \mathbb{1}_{\mathcal{D}_1}(D) + \hat{\omega}_2(V, D) \cdot \mathbb{1}_{\mathcal{D}_2}(D)$ . Two dashed vertical lines indicate wind direction that is parallel to the line connecting the pair of turbines. (Reprinted with permission from Hwangbo et al. [98].)

TABLE 8.4 Wake depth and width for the six pairs of turbines.

	Pair 1	Pair 2	Pair 3	Pair 4	Pair 5	Pair 6
Depth: Turbine 1	41.6% (60.2%)	35.4% (41.8%)	26.6% (36.8%)	26.3% (41.1%)	40.0% (43.8%)	39.1% (44.3%)
Depth: Turbine 2	50.9% (56.2%)	29.2% (33.6%)	43.5% (44.8%)	33.5% (44.8%)	31.1% (44.5%)	42.1% (47.9%)
Width: Turbine 1	40.1°	42.7°	57.8°	51.6°	41.6°	57.5°
Width: Turbine 2	57.0°	52.8°	44.7°	45.6°	47.0°	49.9°

discrepancy between a bearing and the actual wind direction with the highest wake loss—see Fig. 8.7, middle-right panel, for an extreme example.

Table 8.4 shows the wake characteristics for the six turbine pairs. The first two rows are the estimates of wake depth, namely the magnitude of the wake power losses. The last two rows are the estimates of wake width. The wake depth is identified as the peak of the wake loss estimate representing the maximum power loss. The wake width is supposed to be determined by the angles around the bearings at which the power loss eventually becomes zero. However, given noisy signals spreading over a large range of wind directions, the fitted wake power loss is not completely zero even in the regions where it is unquestionably wake free. To estimate the wake width, Hwangbo et al. [98] use the range of wind direction for which loss is greater than 1% of the rated power of the turbine. For the wake depth, Table 8.4 presents two percentage values for each turbine. The one outside the parenthesis is the wake power loss relative to the rated power of that turbine, whereas the one inside the parenthesis is the loss relative to the free-stream equivalent power output.

In the literature, the wake power loss is often expressed as the ratio of the loss over the free-stream equivalent power output [2, 13, 85], which can be computed by

$$\frac{\hat{\omega}_t(V_i, D_i)}{\hat{y}_t(V_i, D_i) + \hat{\omega}_t(V_i, D_i)}, \quad t = 1, 2, \quad i = 1, \dots, n, \quad (8.22)$$

where  $\hat{y}_t(V_i, D_i)$  denotes the expected power generation given  $(V_i, D_i)$ . Depending on  $(V_i, D_i)$ ,  $\hat{y}_t(V_i, D_i)$  could be the expected power in the wake of another turbine, so that the free-stream equivalent power output is to be recovered by adding  $\hat{y}_t(V_i, D_i)$  and  $\hat{\omega}_t(V_i, D_i)$ . To calculate  $\hat{y}_t(V_i, D_i)$ , Hwangbo et al. [98] define a neighborhood of  $(V_i, D_i)$ , i.e.,  $\mathfrak{N}_i = \{(V, D) : V \in (V_i - \epsilon_V, V_i + \epsilon_V], D \in (D_i - \epsilon_D, D_i + \epsilon_D]\}$ , and compute  $\hat{y}_t(V_i, D_i)$  by taking the average of the power outputs whose corresponding wind speed and direction is a member of  $\mathfrak{N}_i$ . This is a two-dimensional binning with  $2\epsilon_V$  and  $2\epsilon_D$  as the respective bin width, where  $\epsilon_V$  and  $\epsilon_D$  are predetermined constants. In this application, Hwangbo et al. set  $\epsilon_V = 0.25$  m/s and  $\epsilon_D = 2.5^\circ$ . The second

TABLE 8.5 Annual power loss for the six turbine pairs.

	Percentage measure (%)					
	Pair 1	Pair 2	Pair 3	Pair 4	Pair 5	Pair 6
Turbine difference ( $\tilde{\eta}_{2-1}$ )	0.26	1.10	0.21	-1.40	3.41	0.94
Wake loss: Turbine 1 ( $\omega_1$ )	0.85 (1.67)	0.78 (1.62)	0.51 (1.13)	0.64 (1.42)	0.59 (1.27)	0.66 (1.33)
Wake loss: Turbine 2 ( $\omega_2$ )	2.00 (4.04)	1.24 (2.69)	1.39 (3.15)	1.11 (2.40)	1.01 (2.36)	1.75 (3.68)
Average wake loss for the pair	1.43 (2.84)	1.01 (2.14)	0.95 (2.13)	0.88 (1.92)	0.80 (1.19)	1.20 (2.48)

percentage values in Table 8.4, i.e., the ones inside the parentheses, are the wake power loss expressed in this conventional fashion.

The peak power loss relative to the free-stream equivalent (the value inside the parenthesis) ranges from 34% to 60%. The wake width for the 12 turbines ranges from 40° to 58° with concentration around 40°–53°. The wake depth commonly stated in the literature is in the range of 30%–40% [12, 14, 192], which appears to be at the lower side of the spline wake model-based estimates. In addition, the new wake width estimates are noticeably larger than the 25° to 40° range stated previously [14, 146, 215]. The difference can be attributed to two major factors. The first one is that the new estimation can identify the wake region more accurately, producing better estimates of the two main characteristics, whereas the methods in the literature rely on *ad hoc* data segmentation and partition and often use a partial set of data based on a pre-selected range of wind direction. Consequently, the previous wake power loss estimates do not capture the characteristics as well as the new estimator does. The second factor is that the historical estimates are usually the averages over multiple turbines, understandably leading to a narrower range.

Table 8.5 shows how each term in the power difference model of Eq. 8.6 affects the power generation of a turbine pair in an annual period, namely the AEP power difference or AEP loss. The first row is the between-turbine power production difference independent of wake effect, expressed relative to the rated power. The second and third rows present the wake loss. Similar to Table 8.4, the values outside the parentheses is the loss relative to the rated power, whereas the values inside the parentheses is the loss relative to the free-stream equivalent. Both percentages represent the AEP wake loss but use different baselines.

The wake loss relative to the rated power is in fact related to the capacity factor of a wind turbine. Recall that the capacity factor is the ratio of the actual power production of a turbine for a selected period of time, say, one

year, over the supposed power production the turbine could have produced, had it operated at its maximum capacity (i.e., at the rated power) all the time; the typical range of the capacity factor is 25%–35%. The wake loss relative to the rated power, therefore, can be seen as the direct reduction to a turbine's capacity factor. Hwangbo et al. [98] refer to the corresponding AEP loss as the capacity factor AEP loss and refer to the AEP loss relative to the free-stream equivalent as the traditional AEP loss. The traditional AEP loss is computed, if using Turbine 1 group as an example, by

$$\frac{\sum_{i=1}^n \hat{\omega}_1(V_i, D_i)}{\sum_{i=1}^n \{\hat{y}_1(V_i, D_i) + \hat{\omega}_1(V_i, D_i)\}}. \quad (8.23)$$

The fourth row is the average AEP wake loss for a pair of turbines. The average is weighted by the number of data points in the respective wake regions to account for the annual distribution of the AEP loss for the turbine pairs. For this reason, the values in the fourth row may be slightly different from the simple average of the two individual losses. The average *traditional AEP loss* for a pair is computed by

$$\frac{\sum_{i=1}^n \{\hat{\omega}_1(V_i, D_i) + \hat{\omega}_2(V_i, D_i)\}}{\sum_{i=1}^n \{\hat{y}_1(V_i, D_i) + \hat{\omega}_1(V_i, D_i) + \hat{y}_2(V_i, D_i) + \hat{\omega}_2(V_i, D_i)\}}. \quad (8.24)$$

The average *capacity factor AEP loss* is computed by setting the denominator in the above equation to be  $\sum_{i=1}^n \{(rated\ power) + (rated\ power)\} = 2n \cdot (rated\ power)$ .

From Table 8.5, one may notice that the magnitude of the between-turbine difference is sizeable, sometimes even larger than that of the wake effect. This result suggests that modeling of the between-turbine difference as a separate term in the power difference model is important to the mission of estimating the wake effect; otherwise, the estimate of the wake effect can be biased considerably.

One can immediately observe that the AEP losses are much smaller than the peak power loss (wake depth). This is expected because the annual loss is the average over all kinds of wind speed and direction conditions in an entire year. Under many circumstances, the wake loss is much smaller than the peak loss. The capacity factor AEP loss is between 0.5–2.0%, meaning that if the turbine's actual capacity factor is 25%, then its ideal capacity factor, if the turbine always operated wake free, could have been 25.5% to 27%. This difference, while appearing as a small percentage, should not be taken lightly. Consider a wind farm housing 200 turbines all in the 2 MW turbine class. A 1% capacity factor AEP loss for the whole farm translates to \$1.3 million annual loss in revenue at the wholesale price of \$37 per MWh.

One may also notice that the wake loss endured by Turbine 2 in a pair is always greater than that of Turbine 1. This can be explained by the relative positions of the turbines and the prevailing wind direction over this farm during that particular year. Fig. 8.8 presents the wind rose plots for three pairs of

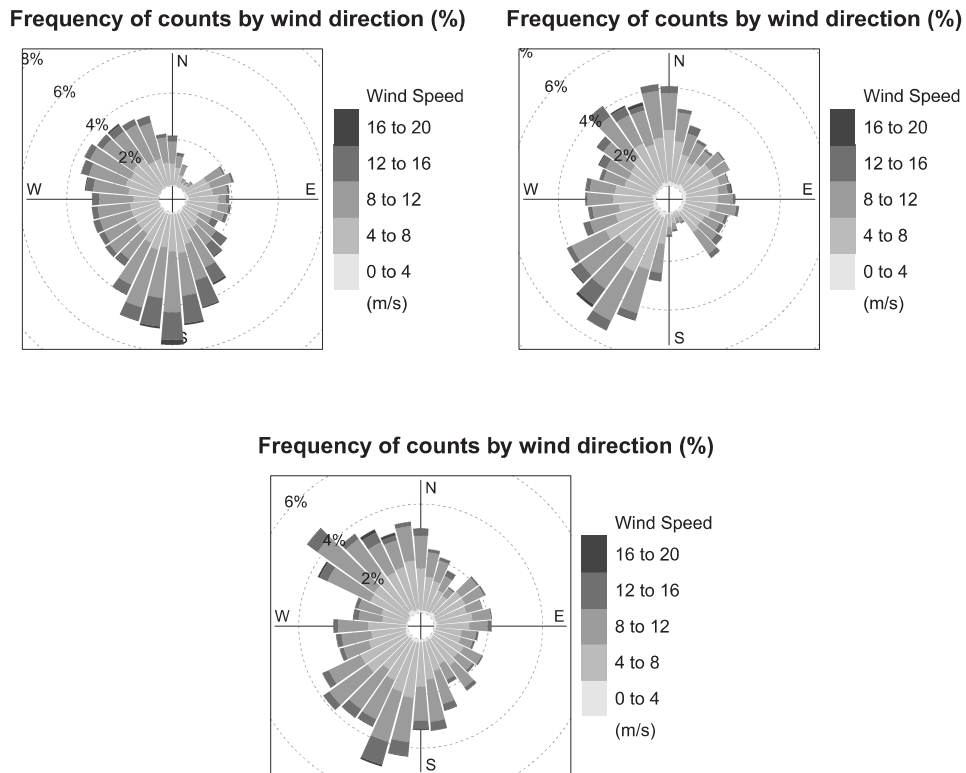


FIGURE 8.8 Wind rose plots illustrating the relative frequency of incoming wind for different direction sectors and for different speed ranges. Top-left panel for Pairs 1 and 2; top-right panel for Pairs 3 and 4; and bottom panel for Pairs 5 and 6. (Reprinted with permission from Hwangbo et al. [98].)

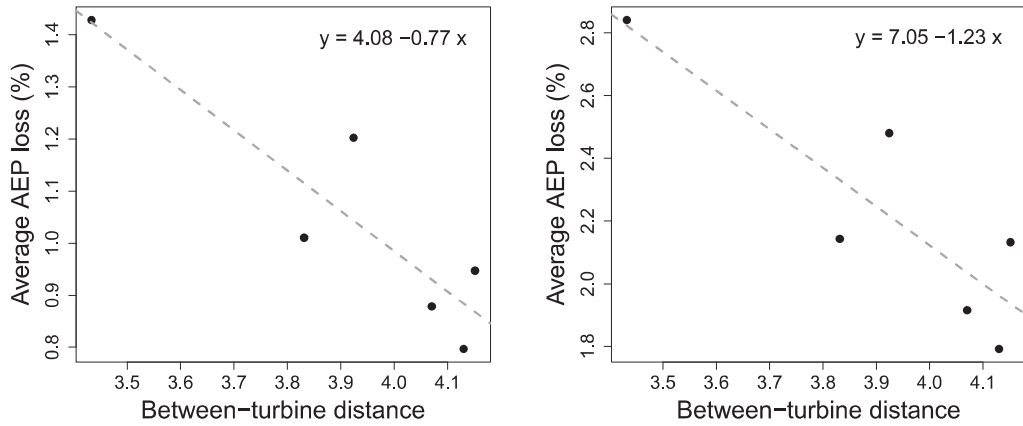


FIGURE 8.9 Relation between AEP losses and turbine spacing. Left panel: for the capacity factor AEP loss; right panel: for the traditional AEP loss. The between turbine distance is expressed as a multiple of the rotor diameter. (Adapted with permission from Hwangbo et al. [98].)

the turbines. The plots show that the northwestern wind, for which Turbine 2 of each pair endures power loss, is more frequent and stronger than the southeastern wind for which Turbine 1 experiences power loss. Unsurprisingly, the AEP loss of Turbine 1 group is usually less than 0.85% (1.67%), whereas the AEP loss for Turbine 2 group is greater than 1.01% (2.36%) and can be as high as 2% (4.04%).

In the literature, it is well known that turbine spacing is a decisive factor affecting the magnitude of wake power loss [13, 129, 192]. Hwangbo et al. [98] conjecture that the variation of the annual power loss between the individual turbine pairs can be explained by the between-turbine distance of each pair. Using the average AEP loss for the six turbine pairs (the fourth row in Table 8.5) and the corresponding between-turbine distances, they fit a simple linear regression model as has been done in [13].

Fig. 8.9 shows the scatter plots and the regression line fitting a respective AEP loss. For the capacity factor AEP loss, the p-values of the intercept and slope estimate are 0.005 and 0.013, respectively. For the traditional AEP loss, the corresponding p-values are 0.006 and 0.022. These results confirm that the turbine spacing indeed by and large explains the pair-wise difference in the AEP losses. An extrapolation based on the fitted regression lines suggests that the wake loss would diminish after the turbine spacing reaches either 5.3 or 5.7 times the rotor diameter, depending on which AEP loss is used in the analysis. Nevertheless, in either circumstance, the 10 times rotor diameter separation used in this study to isolate a particular turbine pair from the rest of turbines appears safe enough to render the turbine pairs free of wake of any other turbines on the wind farm.

Regressing the turbines' inherent production difference (the first row in Table 8.5) on the between-turbine distance, on the other hand, suggests that there is no significant correlation between them. The p-values of the intercept and slope estimate in this case are 0.81 and 0.77, respectively. Unlike the wake effect, the between-turbine production difference does not seem to be affected by the between-turbine distance, much as expected.

## GLOSSARY

---

**AEP:** Annual energy production

**CFD:** Computational fluid dynamics

**GAM:** Generalized additive model

**GMRF:** Gaussian Markov random field

**IEC:** International Electrotechnical Commission

**MAE:** Mean absolute error

**MCMC:** Markov chain Monte Carlo

**RMSE:** Root mean squared error

**TPRS:** Thin plate regression spline

**TPRS-N:** Thin plate regression spline model with non-negativity constraint

## EXERCISES

---

- 8.1 In Section 8.6.1, Jensen's model is used in the form of  $V_{\text{wake}} = (1 - \kappa_{\text{deficit}}) \cdot V$  with  $\kappa_{\text{deficit}}$  being set to 0.075. What if Jensen's model used in the comparison follows Eq. 8.1 instead? Can you update the power difference prediction result in Tables 8.2 and 8.3?
- 8.2 One modeling strategy mentioned and compared with by both Hwangbo et al. [98] and You et al. [232] is the individual turbine power production model, very much like the power curve model introduced in Chapter 5. The individual turbine model in Hwangbo et al. [98] and You et al. [232] is referred to as IND and follows the model structure of

$$y_t = G(\boldsymbol{x}, \boldsymbol{\beta}_t) + \varepsilon_t,$$

which appears similar to the global term in Eq. 8.17 but here  $\boldsymbol{\beta}_t$  is no longer the same for all turbines but tailored to individual turbines. For model performance comparison with IND, please refer to [98, Table 3]. In this exercise, please use the AMK model (Section 5.2.3) as the individual turbine power production model. This is to say, fit the AMK model to two turbines in a pair, respectively, and then compute the power difference. Compare this AMK-based IND model performance with other methods in Tables 8.2 and 8.3.

- 8.3 In Section 8.6.1, when the data binning approach is applied, the wind speed range used in Step 2 is the whole wind speed spectrum. Please use a narrower wind speed range instead and see what difference this change makes in terms of the power difference prediction errors. Two narrower wind speed range options mentioned in Section 8.3 are: (a)  $8.0 \pm 0.5$  m/s and (b) 5.0–11.0 m/s. Furthermore, please investigate the sensitivity of the data binning approach to the width of wind direction bins. Try and compare the bin-width options of  $2.5^\circ$ ,  $5^\circ$  (the current option),  $10^\circ$ , and  $15^\circ$ , in terms of power difference prediction errors.
- 8.4 In Section 8.6.1, Jensen's model is paired with the IEC binning power curve model to compute the power output. What if the IEC binning power curve model is replaced with the AMK-based power curve model (Section 5.2.3)? Conduct the numerical analysis and see how much it affects the power difference prediction errors.
- 8.5 In Section 8.6.2, a linear regression model is built to regress the average wake power loss on the between-turbine distances. It was also mentioned there that one can regress the between-turbine difference,  $\tilde{\eta}$ , on the between-turbine distances and would not find significant correlation between the input and output. Please build the linear regression model and present the scatter plot and the line fit like those in Fig. 8.9.
- 8.6 Use the **Wake Effect Dataset** and the spline-based single-wake model to investigate the sensitivity of parameter  $k$  in that model. Try five different  $k$  values: 10, 20, 30, 40, and 50. Please present a plot displaying how the RMSE and MAE values vary with different  $k$  values. What conclusion do you draw from the plots?
- 8.7 Chapter 6 considers the problem of shape-constrained curve fitting, in which an S-shape constraint is imposed. Chapter 8 considers the problem of sign-constrained curve fitting, in which a non-negativity constraint is imposed. In some circumstances, a shape constraint can be expressed as a sign constraint under a functional transformation, and vice versa. Please show that shape constraints like monotonicity, convexity, or concavity can be expressed as a sign constraint of non-negativity or non-positivity. Please state clearly what type of functional transformation is used to make such equivalence possible.



**Taylor & Francis**  
Taylor & Francis Group  
<http://taylorandfrancis.com>

# III

---

## Wind Turbine Reliability Management



**Taylor & Francis**  
Taylor & Francis Group  
<http://taylorandfrancis.com>

---

# Overview of Wind Turbine Maintenance Optimization

---

Part III of this book discusses a few issues related to turbine reliability management. In this part, the data science problem often concerns modeling and estimating  $f(z|\boldsymbol{x})$ , where  $z$  is the mechanical load measured at certain critical spots on a turbine component, such as at the root of the turbine blades. While the conditional density,  $f(z|\boldsymbol{x})$ , resembles that of  $f(y|\boldsymbol{x})$ , one unique aspect in Part III is that reliability analysis focuses much more on the tail of  $f(z|\boldsymbol{x})$ , rather than on the middle region surrounding its mode. In this sense, reliability analysis concentrates on rare events, which take place with a rather small probability. One important branch of data science methodologies pertinent to reliability analysis is random sampling. Chapters 10 and 11 discuss, respectively, the use of Markov chain Monte Carlo methods and importance sampling methods in the context of turbine blade load analysis.

Chapter 12, however, touches upon a different topic relevant to the general theme of reliability management—anomaly detection and fault diagnosis. The data science problem of anomaly detection and fault diagnosis falls into the category of unsupervised learning, in which the class label of a data record is not available. The very purpose of anomaly detection or fault diagnosis is to recover as accurately as possible the class label for that data record, based on observations of explanatory covariates in  $\boldsymbol{x}$ . While research has been progressing on anomaly detection and fault diagnosis, specialized methods targeting wind turbines are still in great demand. One thing hindering the development on this front, more so than the other data science aspects discussed in this book, is the lack of availability of fault event data resulting from commercial operations to the research community at large. The reason is rather understandable. Whoever owns the reliability or fault event data tends to guard

those data diligently, as the implication of liability through reliability data is much more direct than through environmental data ( $x$ ) or power production data ( $y$ ). Sometimes, the real owner of this type of data, be it the owner/operator or the turbine's manufacturer, can also become debatable. Even if one party may be willing to share the data with a data science research third party, the other party may not want to divulge. The hydropower plant data used in Chapter 12 is in fact subject to a confidentiality agreement and therefore does not appear among the shared datasets.

Before we proceed with load analysis and anomaly detection in the latter chapters, we start off Part III in the present chapter with a discussion of wind turbine operations and maintenance (O&M), which is in and of itself an important part of reliability management.

## 9.1 COST-EFFECTIVE MAINTENANCE

---

Wind turbine O&M plays an important role and accounts for a major portion in the total cost of energy in wind power production. The US Department of Energy's 20%-Wind-Energy-by-2030 report [218, Figure 2-15] shows that while the O&M cost may be as low as 0.5–0.6 cents/kWh in the early years of a turbine's service, it escalates to 1.8–2.3 cents/kWh after 20 years' service. Analysts have also realized that some early estimates of the wind's O&M cost may have been considerably underestimated. In 2011's second issue of the *Wind Stats Report*, William Manganaro, project manager of NAES Corporation, draws a contrast between the 2010 American Wind Energy Association (AWEA)'s estimate of O&M cost at 2.5 cents/kWh and AWEA's initial estimate of 0.5 cents/kWh [181]. Generally speaking, the O&M cost is estimated to account for 20–30 % of the total energy cost in the land-based, utility-scale wind power generation [48], and for offshore wind, the cost portion of O&M is considerably higher. Dr. Fort Felker, former Director of the National Wind Technology Center, stated in a 2009 speech, under the heading of *Critical Elements for 20% Scenario*, that one such critical element is to reduce the O&M costs by 35% from that year's level [62]. Progresses have been made since then but the 35% reduction is still a long way off.

Reducing the cost of O&M for wind power generation appears to be challenging. Under nonstationary loadings due to wind's stochastic nature, a turbine's drive train, especially the gearbox, is prone to failure. Current O&M practice is reactive in nature and depends heavily on what is commonly known as condition-based monitoring or condition-based maintenance (CBM). The concept of CBM is to collect the online monitoring data, and upon diagnosing a turbine's condition, decide whether and when maintenances are needed. A CBM system may ignore the uncertainty in sensory information and respond aggressively to any potential failure signals as is. Doing so of course triggers some of the maintenance actions prematurely. Premature maintenance does not benefit the bottom line of wind operations, and because of that, rarely is such an overconfident approach taken in industrial practices.

On the other side of the spectrum, due to the imperfection of current diagnosis and reliability assessment, compounded with the high cost to undertake a maintenance action, there is always reluctance to take actions until perhaps when it is too late. Scheduled maintenances are rather popular in the wind industry, meaning that the maintenance schedules are fixed *a priori*, e.g., once every six months. Scheduled maintenances are too rigid, so that it either allows too many failures, if the schedules are infrequent, or costs too much, if the schedules are too frequent. The reality is that rigid and reactive maintenance approaches lead to “*a prevalence of unscheduled maintenance*” [182]. It is apparent that neither the overconfident nor the overcautious approach can produce the optimal cost structure for turbine maintenance.

A key in devising a cost-effective maintenance strategy is to handle the uncertainty in sensory information properly and decide the course of action without over-trusting, nor discrediting altogether, the information dynamically collected. In order to compensate for the uncertainty in sensory information, decision makers resort to crew’s on-site investigations as well as simulations of wind farm operations, both of which are more expensive, either economically or computationally, than just using online sensors with intermittent analysis. A relevant question in a dynamic maintenance scheduling system is when an on-site investigation should be triggered and how simulation outcomes can be used together with the sensory data.

With this objective in mind, a dynamic, data-driven approach provides a useful school of thought and points to a close coupling between modeling and information-gathering. A data-driven approach could trigger the expensive on-site investigations adaptively, only as needed, and dynamically update the mathematical models by injecting the newly collected data, as appropriate. This chapter discusses, in such a context, two turbine maintenance optimization models, one wind farm simulator, and an approximation strategy allowing optimization and simulation to work together in real time.

Fig. 9.1 illustrates the need for cost-effective maintenance and highlights the pursuit of a better balance in decision making in the presence of uncertainty.

## **9.2 UNIQUE CHALLENGES IN TURBINE MAINTENANCE**

The challenges in wind turbine maintenance are primarily caused by the stochastic nature of turbine operation conditions and the uncertainties in the decision variables induced by the stochasticity. Because of the stochasticity, the condition-based monitoring for wind turbine systems runs into difficulties while attempting to pin down the occurrence and severity of a potential fault or failure. Complicating the matter further are the weather constraints and disruptions, as well as the logistic difficulties such as long lead time and long service time. Not surprisingly, a poorly planned maintenance job contributes substantially to the escalation of O&M costs of wind turbine systems.

Weather does constrain maintenance activities. To maximize power gener-

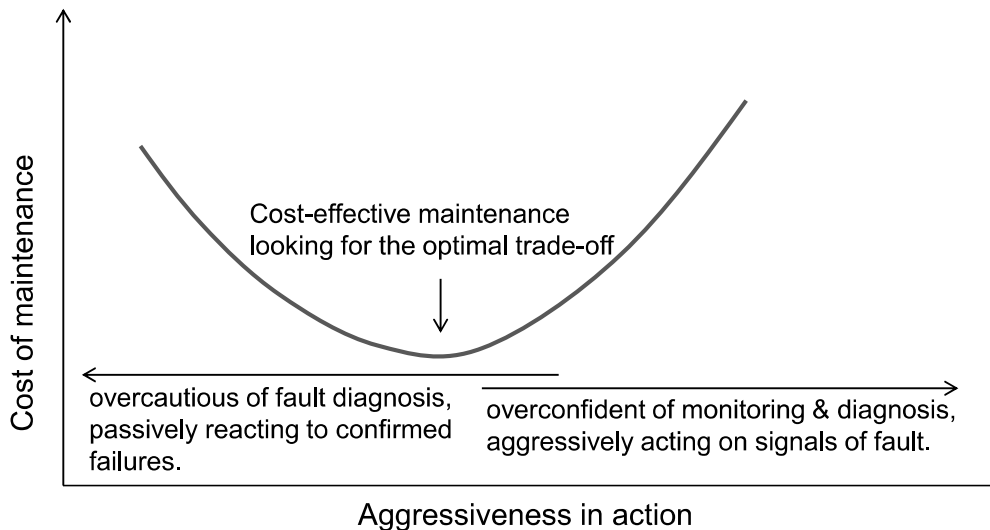


FIGURE 9.1 Plot of cost versus maintenance actions. An overconfident approach, responding to every potential failure signal as if there is no uncertainty, is likely overacting, whereas an overcautious approach, on the other side, likely waits until it is too late to prevent a potential failure.

ation potential, wind farms are built at locations with high wind. But climbing a turbine is not allowed, due to safety concerns, when wind speed is more than 20 m/s. When the speed is higher than 30 m/s, the site becomes inaccessible. The combination of higher failure rates and low accessibility for repairs during windy periods exacerbates the revenue loss because that is the time when wind turbines are supposedly to generate most of its power.

The sheer size of wind turbine components makes it difficult to store spare parts in a warehouse waiting for repairs or replacements. Rather, the large parts are likely ordered and shipped directly from a manufacturer when needed. Doing so leads to long lead time in obtaining parts and can result in costly delays in performing repairs. Pacot et al. [158] state that it may take several weeks for critical parts, such as a gearbox, to be delivered.

The logistic difficulty in turbine maintenance is also caused by the long distances of wind farms from their operation centers, as well as that major repairs require heavy duty equipment, such as a crane or a helicopter, to access the turbine. It certainly takes quite an effort to assemble the maintenance crews and prepare for a major repair. Logistic costs may escalate substantially, depending on the accessibility to the turbine's site, the maintenance strategy, and equipment availability.

The three factors, weather, component size, and distance, can become intertwining with one another, making the already challenging situation even more difficult. For instance, major repair of turbines usually takes weeks to

complete due to the physical difficulties of the job (size and distance). The long duration of a repair session in fact increases the likelihood of disruption by adverse weather.

Besides the effect of wind, as mentioned above, other environmental factors can adversely impact a turbine's reliability, such as extreme low temperature, icing, and lightning strikes, or wave and corrosion for offshore turbines. A comprehensive discussion on this topic can be found in [27].

### 9.3 COMMON PRACTICES

---

The methods of wind turbine maintenance commence rather naturally with analyzing the historical failure data to elucidate a component's failure probability and then plan maintenance accordingly. These are referred to as the failure statistics-based approaches. In the meanwhile, there have been attempts to establish reliability models, based on first principles and/or stochastic process theories, to provide an understanding of the stochastic aging behavior of turbine components. The recent rapid advancements in microelectronics and sensing technology have allowed real-time measurements and analyses of various characteristics of wind turbines during their operations—this line of approaches is collectively referred to as condition-based maintenance.

#### 9.3.1 Failure Statistics-Based Approaches

Failure statistics-based approaches are purely data-driven. Although often applied to individual components, this type of approach can actually be used for the whole turbine as well. The idea is to use the historical failure data to fit certain probability distributions, which then yield a number of commonly used statistics such as the mean time to failure (MTTF) [82, 227]. The popular distribution here, as in reliability analysis in general, is the Weibull distribution, which has been described in detail in Chapter 2 (Sections 2.2.2–2.2.4). In Chapter 2, the Weibull distribution is used to model the wind speed distribution. It turns out that the Weibull distribution is also a common choice in reliability analysis, because like wind speed, the time to failure is positive and right skewed in distribution. In addition to Weibull distributions, analysts also use the non-homogeneous Poisson process to handle the cases where the number of failures is provided but the time when a failure takes place is missing [80, 210, 211]. Analysts build and run Monte Carlo-based simulation models by making use of the statistics and distributions obtained above in order to study or visualize the stochastic behavior of a turbine's failures. Simulations are furthermore conducted for evaluating the effectiveness of maintenance actions, assessing the impact of turbine reliability on power generation, comparing turbine siting choices, and validating operational strategies [28].

### 9.3.2 Physical Load-Based Reliability Analysis

It is desirable that a physical relationship between loads and component failures can be established [131], a topic to be discussed in more detail in Chapters 10 and 11. The load-based reliability analysis refers to the studies concerning the fatigue load or extreme load, or the characterization of wake effect. In Chapter 8, we discuss the impact of wake effect on power production. The wake effect also has an adverse impact on turbines in the form of an increased mechanical load. The load-based analysis has mainly concentrated on the structural components of a turbine, i.e., blades and the tower, and are generally carried out offline. National Renewable Energy Laboratory in the US and Risø National Lab in Denmark, the two leading government organizations in wind technology, have developed their respective structural aeroelastic codes and tools to assess the structural loads using computer-based simulations [112, 113, 130]. The IEC publishes design standards [101] for the structural components of a turbine.

### 9.3.3 Condition-Based Monitoring or Maintenance

CBM involves two necessary analyses: (a) failure modes analysis to understand how the likely failure patterns are associated with the major components in a turbine [177], and (b) analysis of the turbine's operational data acquired by *in situ* sensors for diagnosis and prognosis [230]. Different from the failure statistics-based approach that is done offline, CBM is conducted on a continual, online basis. With the accumulation of online data and advancement in signal analysis, the concept of prognostics and health management has emerged, which is nonetheless within the broad scope of CBM. Although CBM may be used for any components in a wind turbine, the current practice mainly focuses on the drive train, where vibratory responses, acoustic emissions, temperature, and lubrication oil particulate content are the common measurements monitored. Addressing gearbox reliability is one of the major efforts of NREL, who released the Gearbox Reliability Council's report in June 2011 [135].

## 9.4 DYNAMIC TURBINE MAINTENANCE OPTIMIZATION

---

The imperfection of today's diagnosis tools is due to the fundamental limitations in our knowledge of the engineering systems, sensing technologies, and data science methods. Uncertainties are not going to disappear from diagnosis and prognosis anytime soon, and as a consequence, analysts need to systematically address the issue of uncertainties in maintenance decision making. General methodologies enabling decision making under uncertainties have seen advancements. One of them is the Markov decision process (MDP) [170], including the partially observable MDP (POMDP) [137, 141] or hidden Markov process [57], for handling the cases when a system's state is not perfectly ob-

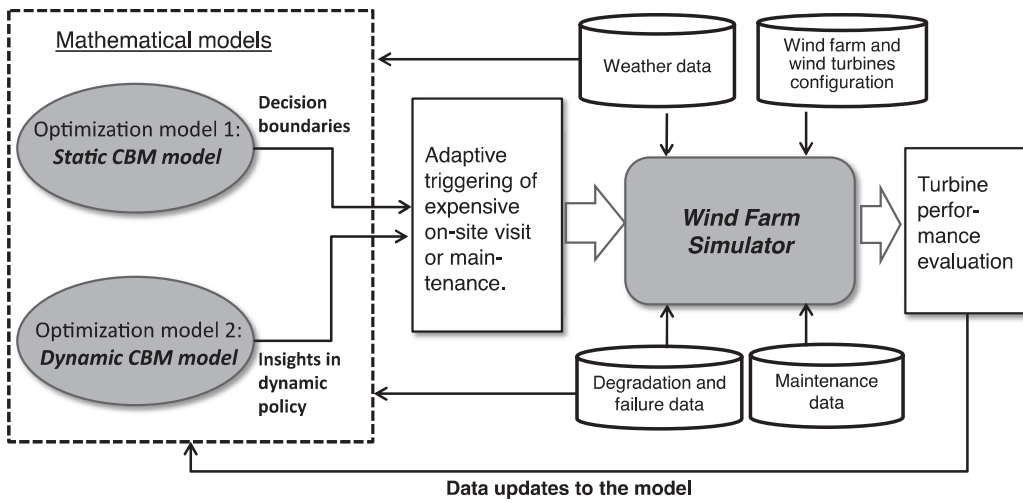


FIGURE 9.2 The framework of the dynamic, data-driven approach for wind turbine maintenance—an integration of models, simulation, and data in a closed loop.

servable due to data or model uncertainties. These methods have been used in traditional power system reliability analysis, like for transformers [110] as well as for wind turbines [25, 26]. The resulting dynamic models consider the stochastic weather constraints and logistic uncertainties as mentioned earlier, and work in an integrated framework with a wind farm simulator to guide model updates and measurement in-taking. A general dynamic maintenance optimization framework is illustrated in Fig. 9.2.

The dynamic maintenance optimization framework includes three important models—two optimization models [25, 26] and a simulation model [28, 161]. The two optimization models come with different flavors: one is a static model whose parameters stay constant, whereas the other is a dynamic model whose parameters are adjusted responding to different seasonal weather patterns. The merit of having both optimization models is that the dynamic model, despite desirable in terms of adaptivity, is expensive to solve, because it is difficult to extract a solution structure due to the complexity of the model. The static model, albeit a simplification of reality, does reveal a solution structure that facilitates solving for maintenance decisions efficiently. The wind farm simulation model is a discrete event-based model, mimicking the operation of a wind farm with hundreds of wind turbines that may degrade along different paths and thus need service at different times. The simulator is specially designed to handle a large number of unorganized random events (e.g., waiting for parts or weather disruptions) and reflect in the simulator's outputs the stochasticity from the operations. The dynamic maintenance optimization framework integrates the optimization models, the simulator, and

the data, in a closed loop where sensor data are used to improve the modeling analysis and prediction.

#### 9.4.1 Partially Observable Markov Decision Process

Byon et al. [25, 26] develop maintenance optimization models based on partially observable Markov decision processes. Part of the reason motivating the use of POMDP is that a turbine’s SCADA data are noisy and the SCADA data can, at best, provide partial information of the turbine’s health status. In the POMDP setting, the system’s degrading condition can only be assessed in a probabilistic sense, represented by the information state  $\pi$ . Suppose that the turbine health condition can be discretized into  $M$  levels, with Level 1 being the best condition like a new turbine and  $M$  being the most deteriorated condition right before failure. Then, the information state can be expressed as  $\pi = [\pi_1, \dots, \pi_M]$ , and each element in the  $\pi$ -vector is a probability, indicating the likelihood of the turbine being at that level. This  $\pi$ -vector is used as an important input to the subsequent POMDP model, so that any decision made is based on a probabilistic assessment, rather than the assumption of knowing to which level the turbine has degraded.

Byon et al. [25, 26] consider  $L$  number of failure modes. Combining with the  $M$  degradation levels, this POMDP model has a total of  $M + L$  states. Out of the  $M + L$  states,  $M$  of them are working states and  $L$  of them are failing states. A turbine transitions through the working states and ultimately arrives at one of the failing states, unless some kind of intervention takes place prior to failure. A turbine does not have to exhaust all working states before it fails—it is possible that a turbine can fail at any working state. Once it arrives at one of the failing states, it stays there and will not transition further to other failing states. A turbine can only go from a failing state back to a working state when a repair or replacement operation is carried out.

Transitions between those states are illustrated in the state transition graph in Fig. 9.3, left panel, where  $P_{ij}$  is the transition probability from state  $i$  to state  $j$ . One may notice that there is no state transition between the  $L$  failing states but there is a link between any working state to a failing state, per discussion in the earlier paragraph.

Cost-effective maintenance trades multiple choices of action. Besides the options of preventive maintenance (PMT) or continue with SCADA monitoring, i.e., do-it-later (DIL), a possible intermediate action is to conduct on-site visit/investigation (OVI), to find out more certainly how a turbine is operating. This on-site action is much more expensive than purely SCADA-based monitoring, considering the long distance between a service center and a wind farm, but less expensive than a fully blown repair job, which employs expensive heavy-duty equipment and a larger crew. Other than the three options, corrective maintenance (CMT), i.e., the reactive action once a failure has already happened, always needs to be considered. Understandably, corrective maintenance is the most expensive among all options.

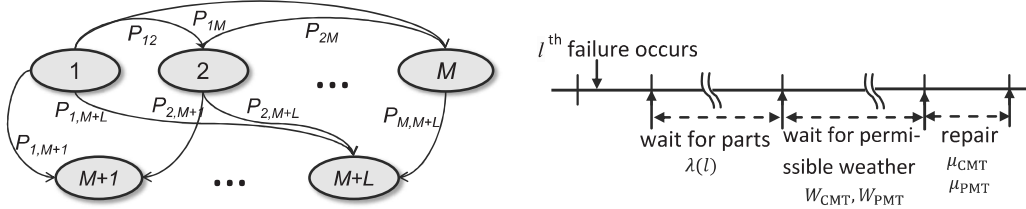


FIGURE 9.3 Maintenance modeling. Left panel: state transition graph and  $P_{ij}$  is a transition probability; right panel: uncertainty caused by weather and logistics. (Left panel reprinted with permission from Byon et al. [27].)

The POMDP model takes a dynamic programming form. At time  $t$ , let  $C_t(\pi_t)$  denote the cost for maintenance until a terminal time (e.g., when the turbine is decommissioned), given that its current state is  $\pi_t$ , and let  $a_t$  denote the action options at  $t$ . If one considers the three options mentioned earlier, then  $a_t$  is chosen from the set of {PMT, OVI, DIL}. According to the theoretical framework of POMDP [141, 170], the optimal solution regarding which action to take can be decided based on the following optimization problem:

$$C_t(\pi_t) = \min_{a_t} \left\{ c_t(\pi_t, a_t) + \gamma \cdot \sum_{\pi_{t+1} \in S} P(\pi_{t+1} | \pi_t, a_t) \cdot C_{t+1}(\pi_{t+1}) \right\}, \quad (9.1)$$

where  $a_t$  is the decision variable to be optimized,  $c_t$  is the immediate cost incurred by taking action  $a_t$ ,  $\gamma$  is the cost discount factor due to the monetary depreciation over time, and

$$S := \{[\pi_1, \dots, \pi_{M+L}], \quad \text{s.t.} \quad \sum_i \pi_i = 1, \quad \pi_i > 0 \quad \forall i\}$$

is the set of information states.

The above optimization formulation is in recursive form, because the minimum value of  $C_t$  depends on that of  $C_{t+1}$ . Modeling  $C_t(\cdot)$  and  $c_t(\cdot)$  for each decision period involves the considerations outlined earlier, such as which action to take and its corresponding cost, when such an action is permissible, and how much revenue loss is incurred due to a turbine's downtime. The solution of the POMDP formulation typically starts from the terminal time, say, at  $T$ , when  $C_T(\pi_T)$  can be decided since the turbine is supposed to have arrived at one of the failing states. Then the action at  $T - 1$  can be solved, which gives the value of  $C_{T-1}(\pi_{T-1})$ . Going further back in time solves for the rest of actions in the turbine's maintenance history.

Byon et al. [25, 26] consider the stochasticity resulting from waiting for permissible weather windows and from repairing, all of which manifest as random events to be included in the decision model; see Fig. 9.3, right panel.

The adverse weather conditions are modeled using two prohibiting probabilities:  $W_{\text{CMT}(l)}$  as the probability that the prevailing weather conditions are so adverse that the corrective maintenance required for the  $l^{\text{th}}$  failure mode,  $l \in \{1, \dots, L\}$ , is not allowed, and  $W_{\text{PMT}(m)}$  likewise defined for a preventive maintenance that is supposed to restore the system back to the  $m^{\text{th}}$  degradation level,  $m \in \{1, \dots, M\}$ . The waiting periods and repair jobs are characterized through a queuing model having its processing rate, respectively, of  $\lambda(l)$ ,  $\mu_{\text{CMT}(l)}$ , and  $\mu_{\text{PMT}(m)}$ .

The costs of different actions are denoted as  $c_{\text{OVI}}$  for on-site visit/investigation,  $c_{\text{PMT}(m)}$  for the  $m^{\text{th}}$  mode of preventive maintenance repair, and  $c_{\text{CMT}(l)}$  for corrective repair upon the  $l^{\text{th}}$  mode of failure. During the downtime until a repair is completed, a revenue in the amount of  $\tau_t$  is lost.

With these parameters and settings, the cost and probability items in the dynamic programming formulation in Eq. 9.1 can be uniquely specified. For instance, the consequence associated with  $\text{PMT}(m)$  at time  $t$  can be expressed as

$$\begin{aligned} \text{PMT}_t(m) = & W_{\text{PMT}(m)}(\tau_t + \text{PMT}_{t+1}(m)) + \\ & (1 - W_{\text{PMT}(m)})[\tau_t + c_{\text{PMT}(m)} + C_{t+1}(e_m)], \end{aligned} \quad (9.2)$$

where  $e_m$  is one of the extreme states of which the  $m^{\text{th}}$  element in  $[\pi_1, \dots, \pi_M]$  is *one* and all other elements are *zeros*. The notation,  $\text{PMT}(m)$ , denotes the cost associated with the preventive maintenance action restoring a more degraded turbine system to the state  $e_m$ . The interpretation of the above equation is that the preventive maintenance cost at  $t$  to restore the turbine to state  $e_m$  is affected by the weather condition. When the weather condition is not permitting for this type of action, with a probability of  $W_{\text{PMT}(m)}$ , the preventive maintenance action will then have to wait until the next period. While waiting, the turbine incurs a production loss of  $\tau_t$ . If the weather condition is permitting, with a probability of  $1 - W_{\text{PMT}(m)}$ , and the preventive maintenance action is in fact completed, then the costs incurred are the production lost during the repair period, the cost associated with the specific repair action  $\text{PMT}(m)$ , and the cost of operation for the next period with the turbine in the state of  $e_m$ .

#### 9.4.2 Maintenance Optimization Solutions

If one assumes that all the weather-associated parameters in the dynamic programming model in Eq. 9.1 are constant over time, the solution of the dynamic programming model then corresponds to a static maintenance system. One may solve the optimization model offline using the value iteration or policy iteration method [170]. The solution outcome is a decision map, allowing analysts to trade off the three major maintenance actions, namely PMT, DIL, and OVI, based on an online estimation of a turbine's degradation status (coded in  $\pi$ ). This maintenance decision process is labeled *static*, because the

decision map stays the same, even though the estimation of  $\pi$  changes (move from  $\pi_t$  to  $\pi_{t+1}$  over time). Fig. 9.4 illustrates how the offline optimization and online sensory information work together.

Albeit a simplification of the reality, the static maintenance model does allow analysts to understand the structure of the maintenance policy with clarity. Fig. 9.5 depicts how a maintenance action is selected. Simply put, it depends on the relative costs of the respective actions. The aging status of the turbine system is one of the primary forces driving the cost structure. When a turbine system is relatively new, the cost associated with DIL option is low, as the chance that the system has a catastrophic failure is low in the near future. As a turbine system ages, the chance of failing gets higher, and the consequence of a failure becomes more serious. The choice between doing an on-site investigation versus doing a fully blown maintenance depends on the cost difference between the two options. For older turbines, the choice of full-blown maintenance action is taken most seriously.

The decision maps, as shown in Fig. 9.6, have three action zones. The decision boundary between two decision zones corresponds to the boundary point in Fig. 9.5 between a pair of actions. The two plots in the upper panel of Fig. 9.6 are decision maps produced by a static maintenance model in which the model parameters are kept constant for the entire decision horizon. Under the static model structure, analysts can decide the decision boundaries analytically and populate a decision zone with its respective decision. The difference between the two upper-panel plots is due to the use of different prevailing weather parameters, namely that  $W_{\text{PMT}}$  and  $W_{\text{CMT}}$  are under different values. In the left column,  $W_{\text{PMT}} = 0.1$  and  $W_{\text{CMT}} = 0.3$ , whereas in the right column,  $W_{\text{PMT}} = 0.5$  and  $W_{\text{CMT}} = 0.5$ . Apparently, the resulting decision map changes when the weather becomes more prohibiting, as the weather conditions in the left figure turn into that in the right figure. The right figure has a higher probability that an ongoing maintenance may be disrupted, and accordingly, the decision zones of PMT and OVI shrink, whereas the zone of DIL expands, suggesting that one needs a higher confidence of potential failures to undertake more expensive actions.

When the maintenance model uses time-varying parameters, it becomes a dynamic model, which is a better reflection of the reality, as the actual system and the environment constantly change. The difficulty of handling a dynamic model is that the exact solutions will have to be found through iterative numerical procedures. Understandably, these iterative numerical procedures are not computationally cheap to use. The two plots in the lower panel of Fig. 9.6 are decision maps from a dynamic model. As seen in the plots, the dynamic model can produce a path of maintenance policies, rather than identify the decision boundaries delineating the decision zones. To solve for the path of a maintenance policy, Byon and Ding [25] use the backward dynamic programming procedure, as outlined in Algorithm 9.1.

If one looks at the plots in the upper and lower panels of Fig. 9.6, it is not difficult to notice that the policy structure implied by the static maintenance

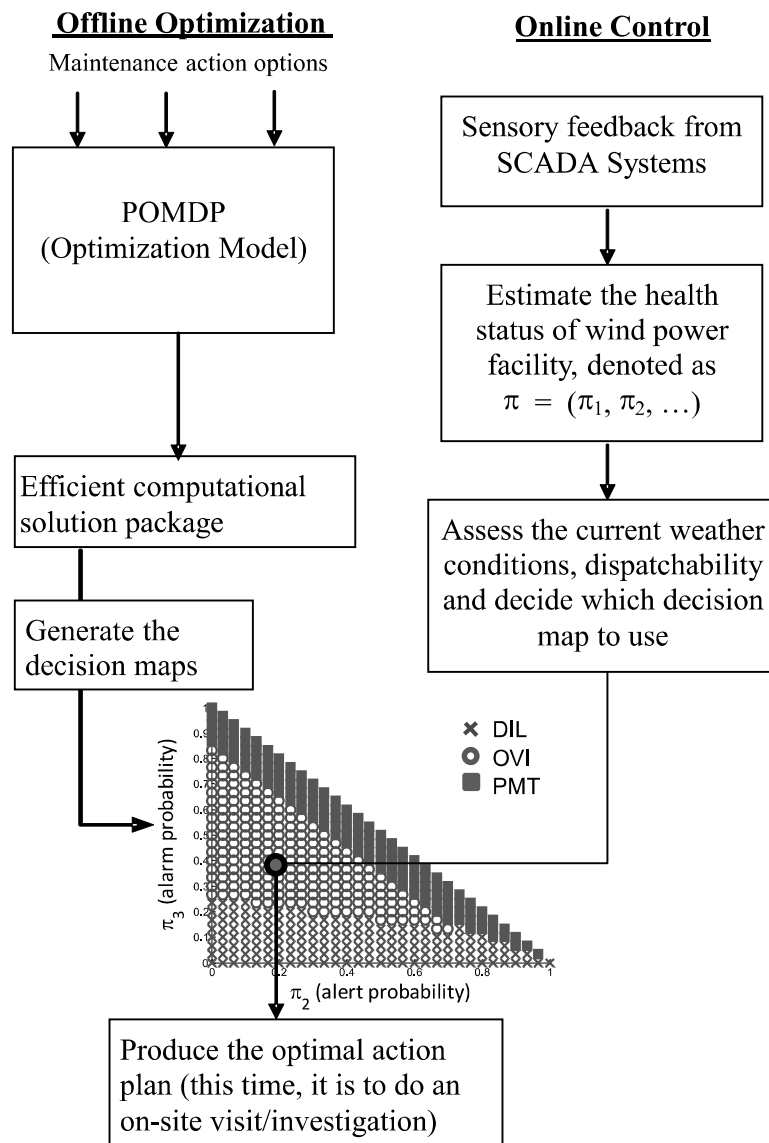


FIGURE 9.4 Offline optimization generates the decision map, while online observations allow an assessment of turbine degradation status. Together they produce the cost-effective maintenance decision.

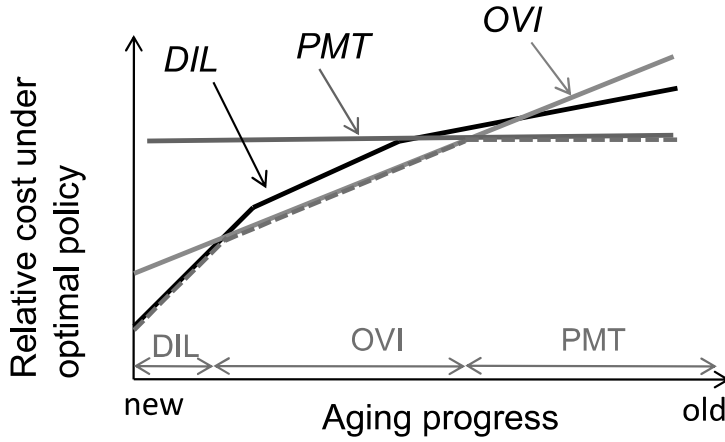


FIGURE 9.5 Maintenance decision structure. When a turbine system is relatively new, the optimal action tends to be do-it-later, as the risk of a catastrophic failure is low. When a turbine system ages, the consequence of a failure gets more serious, so that more aggressive actions are needed. (Adapted with permission from Byon et al. [26].)

---

**Algorithm 9.1** Backward dynamic programming solution procedure.

---

1. Construct a sample path emanating from  $\pi$ , as well as the extreme sample paths originating from the extreme states  $e_m$ ,  $m = 1, \dots, M$ .
  2. Set the turbine's decommission time as  $T$  and the decommission value as  $C_T(\pi)$ , based on a specific system preference.
  3. Set  $t = T - 1$ .
    - (a) Update parameters such as  $W_{\text{CMT}(l),t}$ ,  $W_{\text{PMT}(m),t}$  and  $\tau_t$ ,  $l = 1, \dots, L$ ,  $m = 1, \dots, M - 1$ .
    - (b) Find the optimal decision rule and optimal value at extreme points  $e_i$ ,  $i = 1, \dots, M$ .
    - (c) Compute  $\text{CMT}_t(l)$  and  $\text{PMT}_t(m)$  for each corrective maintenance and preventive maintenance option, as well as that for  $\text{DIL}_t(\pi)$  and  $\text{OVI}_t(\pi)$ , respectively.
    - (d) Compute the optimal value function,  $C_t(\pi)$ , and the corresponding optimal decision rule.
    - (e) Set  $t = t - 1$ , and go back to (a).
-

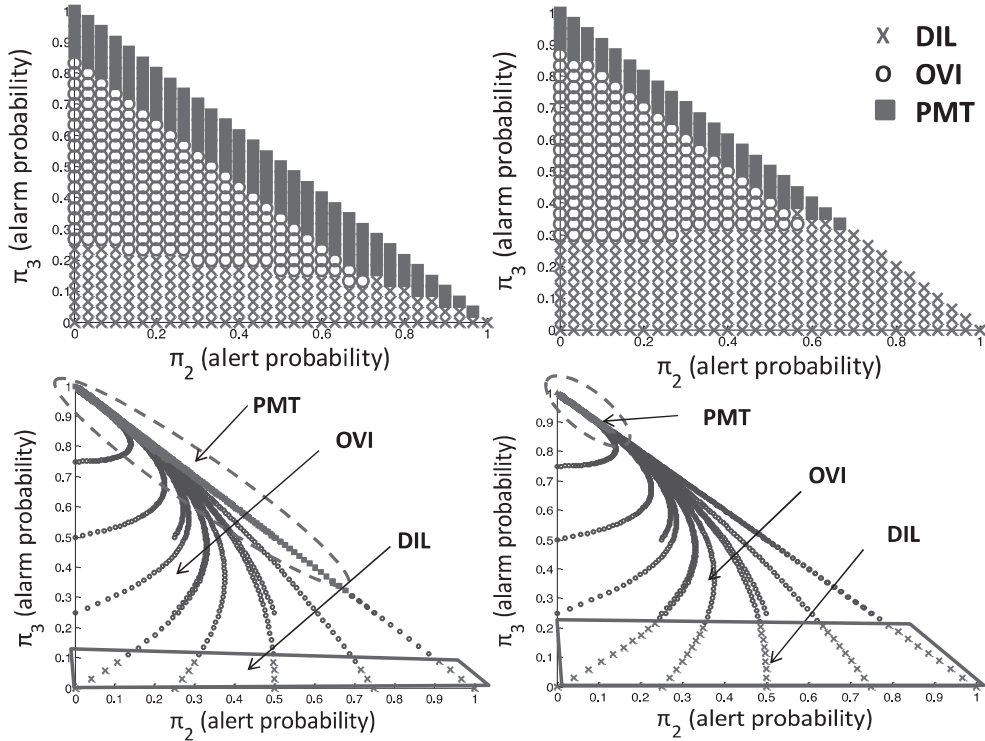


FIGURE 9.6 Static and dynamic maintenance model solutions. Upper panel: static model solutions; lower panel: dynamic model solutions. The two plots in the left column are under the weather condition with  $W_{PMT} = 0.1$  and  $W_{CMT} = 0.3$ , whereas the two plots in the right column are under  $W_{PMT} = 0.5$  and  $W_{CMT} = 0.5$ .

model are more or less preserved in the dynamic model outputs, although the precise decision boundary would have almost surely shifted to a certain extent, as the model parameters are not exactly the same under the static and dynamic circumstances. Upon this revelation, Byon [24] deems it a sensible approach to solve the dynamic model faster and in real time through the following approach: derive useful approximations in the maintenance policy structure based on the static model, employ the resulting structure to pre-partition the decision map, and invoke the numerical solution procedure only when a decision gets close to the prescribed boundary line.

#### 9.4.3 Integration of Optimization and Simulation

One merit of the POMDP-based maintenance models presented in the preceding sections is that they explicitly model the external environmental conditions under which a turbine system is being operated. The static model, because of its stronger assumptions, may be useful for wind farms that operate in

relatively stationary weather conditions, whereas the dynamic model is more adaptive even when there are strong seasonal variations.

Both models nonetheless focus on a single turbine. To the best of our knowledge, using the single-turbine models is the case for the majority of turbine maintenance research [27]. This is not surprising, as building and solving an optimization model for a single turbine is already challenging work, and doing so for a commercial size wind farm housing one hundred plus wind turbines could be analytically intractable.

Maintenance strategies devised based on a single turbine may still be useful to advising operations and decisions on a wind farm. The potential problem is that the randomness in turbine degradation processes cause different turbines to follow different degrading paths, thereby creating a need to adjust maintenance actions accordingly and to resolve the conflicts caused by the multi-turbine environment.

To address this issue, Byon et al. [28] and Pérez et al. [161] develop a discrete event system specification (DEVS) [233]-based simulation platform for a wind farm housing many wind turbines. The specific simulation framework, DEVS, is selected because using it enables an easier modeling of multi-scale (time, space and decisions) complex systems. DEVS is a formal modeling and simulation framework based on dynamical systems theory, providing well-defined concepts for coupling atomic and coupled models, hierarchical and modular model construction, and an object-oriented substrate supporting repository reuse. Under the DEVS framework, each turbine is treated as a duplicable module, so that the simulation can be scaled up without difficulty to more than one hundred turbines for a farm. Each turbine module includes a turbine components sub-module, degradation sub-module, power generation sub-module, sensing and maintenance scheduling sub-module. Fig. 9.7 presents a high-level diagram of the DEVS-based wind farm simulation.

After the turbine module is built, one also needs to define the logic that interconnects components in a wind turbine system and mimics the execution and operation in a virtual, cyberspace environment. The simulator is designed to handle a large number of unorganized random events (turbine failures, waiting for parts, weather disruptions) and reflect in the simulator's outputs the stochasticity from the operations.

On the one hand, there are two turbine-based optimization models that can advise on optimal maintenance actions for a single, specific turbine, while on the other hand, there is a wind farm simulator used to evaluate the effectiveness of the resulting maintenance decisions on multiple turbines following different degradation paths, to suggest update and adjustments if necessary. It becomes apparent that one would need to integrate the optimization models and the simulation model in order to materialize the dynamic turbine optimization framework, as highlighted in Fig. 9.2.

Integrating the dynamic MDP model with the wind farm simulator is not trivial, as it creates a computational challenge. Recall that the optimal policy in the dynamic model is solved through a backward dynamic programming

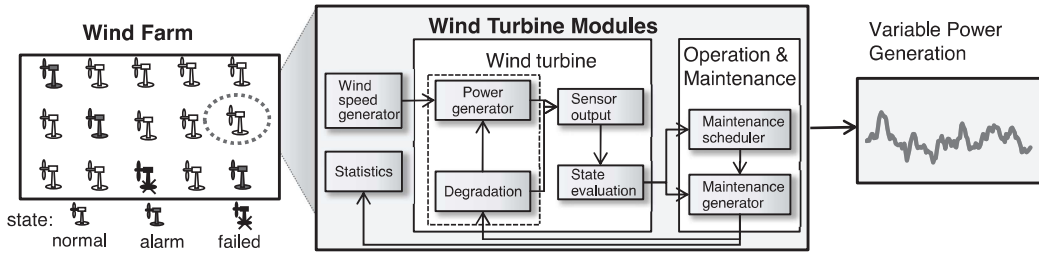


**FIGURE 9.7** The hierarchical structure and operation of the DEVS-based wind farm simulator. Each turbine is treated as a duplicable module, which includes sub-modules such as turbine components, degradation, power generation, sensing and maintenance scheduling.

algorithm that is computationally demanding for large-scale problems. When every turbine needs to run this computational procedure in the wind farm simulator for its decision on maintenance, the simulator creeps to a halt.

To alleviate this problem, Byon [24] proposes an approximation approach, taking advantage of an observation made in the previous section, i.e., the decision map from the dynamic model preserves the structure of optimal maintenance policy revealed by the static model. Byon further conjectures that a set of similar decision rules established from a static model may be used to closely *approximate* a dynamic policy. Because this set of rules is rooted in the static policy, they can be expressed in closed form, and their computation leading to decision boundaries can be done in real time.

Fig. 9.8 illustrates how to approximate the dynamic policy based on a set of decision rules derived from a static model. Firstly, Byon [24] adjusts the cost component associated with a maintenance action and makes it updateable with real-time information on weather (characterized by parameters  $W_{PMT}$  and  $W_{CMT}$ ), logistics (characterized by  $\lambda$ ), and revenue loss (characterized by  $\tau$ ). Note that for a variable energy source like wind, its revenue loss due to downtime also depends on wind input and may vary over time. Secondly, Byon updates the static decision boundary by plugging in the new dynamic cost obtained. This plug-in is the part of approximation. When an action mismatches with the theoretical optima, the maintenance cost elevates, as compared to the theoretically optimal level. Numerical studies conducted in [24] show, however, that the mismatch rates are around 5% of the decision regions. When costs over different scenarios are considered, the impact of this 5% mismatch is translated to less than 1% increase in terms of maintenance cost. The benefit of using this simple set of approximations reduces the computation remarkably, a 98% reduction as compared to the use of the dynamic programming solution procedure [24]. On balance, Byon states that this approximation approach produces significant benefits and allows the integration of the optimization models and the wind farm simulator in an online decision support fashion.

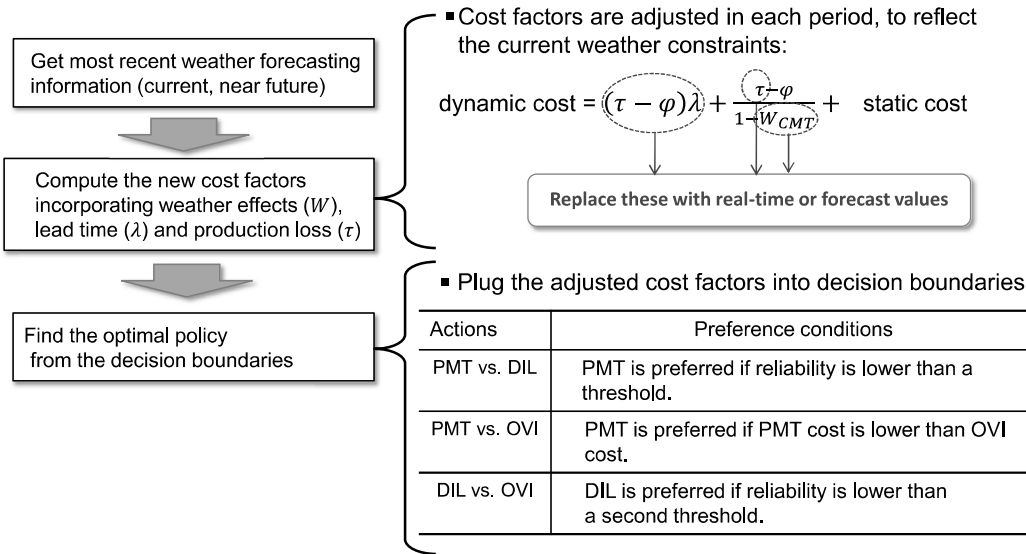


FIGURE 9.8 Approximating the maintenance policy and making it real-time executable. The variable  $\varphi$  indicates the average cost per period.

When executing the integrated framework, real-time weather information or its forecasts in near future are to be used to update the decision boundaries as the simulator runs. This is where wind field analysis and wind forecasting methods in Part I of this book can chime in and benefit the overall wind engineering decision making.

Byon [24] implements this dynamic condition-based maintenance policy for a prototypical wind farm and compares the outcomes with those using scheduled maintenance, a popular practice in industry. The numerical study in [24] shows that using a well-devised dynamic policy leads to a 45% reduction in the annualized failure rate and the number of preventive repairs, and a 23% reduction in the overall maintenance cost. These comparison outcomes are charted in Fig. 9.9.

## 9.5 DISCUSSION

This chapter presents an overview of a dynamic maintenance optimization paradigm for wind turbine systems. One great challenge in wind turbine maintenance is the non-steady loading and stochasticity in the environment conditions under which turbines operate. These factors drive wind turbines to a fast degradation process, cause the fault diagnosis and condition monitoring to have low specificities, and render any rigid maintenance paradigms costly—all hurt wind energy’s market competitiveness. The dynamic, data-driven maintenance approach, with its adaptiveness to a varying environment, strikes a cost-effective balance among different competing cost factors and optimizes for the long-run benefit in the presence of data and model uncertainty.

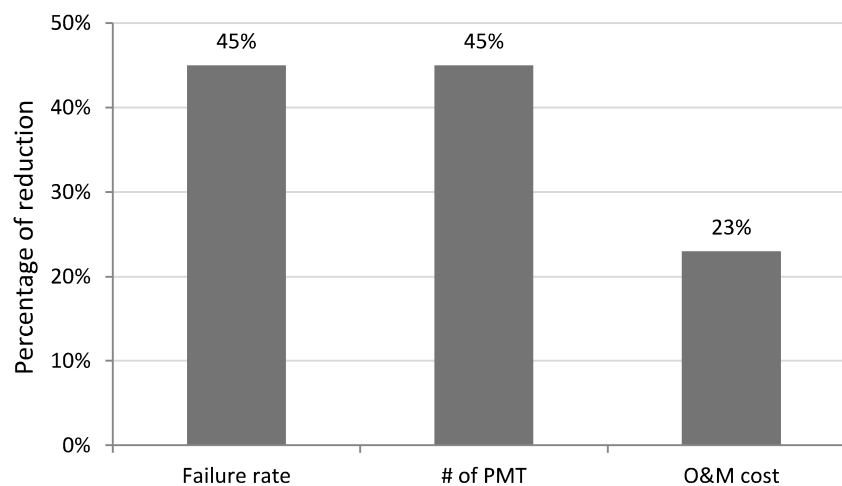


**FIGURE 9.9** Benefit of the dynamic turbine maintenance optimization as compared to scheduled maintenance. Shown in the plot is the reduction in terms of the failure rate, number of maintenance actions, and overall O&M cost.

The virtue of a dynamic maintenance framework can be understood in three aspects: (a) It incorporates real-time measurements, learns what the data reveals, and updates the models as needed; (b) it pays full attention to the uncertainty of information, and promotes the use of multi-accuracy information sources (SCADA versus on-site investigation) to compensate for the adverse effect resulting from information uncertainty; and (c) it combines multi-fidelity models (static, dynamic, and simulation) in an integrative fashion, which enables decisions to be made both efficiently and effectively.

Presenting this framework at the beginning of Part III serves as a bridge connecting the wind forecasting work in Part I, the turbine performance analysis work in Part II, and the load analysis and anomaly detection work to be covered in the remaining chapters in Part III.

## GLOSSARY

---

**AWEA:** American Wind Energy Association

**CBM:** Condition-based monitoring or condition-based maintenance

**CMT:** Corrective maintenance

**DEVS:** Discrete event system specification

**DIL:** Do it later

**IEC:** International Electrotechnical Commission

**MCMC:** Markov chain Monte Carlo

**MDP:** Markov decision process

**MTTF:** Mean time to failure

**NREL:** National Renewable Energy Laboratory

**O&M:** Operations and maintenance

**OVI:** On-site visit and investigation

**PMT:** Preventive maintenance

**POMDP:** Partially observable Markov decision process

**SCADA:** Supervisory control and data acquisition

**s.t.:** Such that

**US:** United States

## EXERCISES

---

9.1 Consider a turbine system which has only two states, up (operating state) and down (failure state).

- What are the values of  $M$  and  $L$ ? What is the dimension of the transition probability matrix  $\mathbf{P} = (P_{ij})$ ? Recall that the transition probability matrix is denoted by  $\boldsymbol{\Pi}$  in Eq. 4.6. Here  $\mathbf{P}$  is used in the place of  $\boldsymbol{\Pi}$  because  $\pi$  in this chapter is used to denote the information state, rather than the transition probability.
- Can you draw the state transition diagram like in Fig. 9.3, left panel?
- Let  $\lambda$  denote the failure rate, which is the probability that the turbine fails and let  $\mu$  denote the probability with which a failing system can be restored to the operating state. Write down the corresponding transition probability matrix  $\mathbf{P}$ .
- What are the mean time to failure and the mean time to repair for this system?

9.2 Can you write down the costs associated with other action options, i.e., OVI, DIL, and CMT, like what was done for PMT in Eq. 9.2?

9.3 The probability that a system will still operate until the next decision point is called the reliability of the system and denoted by  $\Upsilon(\pi) = \sum_{i=1}^M \sum_{j=1}^M \pi_i P_{ij}$ . Express the information state after the next transition,  $\pi'$ , in terms of the current state,  $\pi$ , and the reliability of the system, provided that the system has not yet failed.

- 9.4 The preventive maintenance cost expressed in Eq. 9.2 is for a major repair action. For a minor repair, there are at least two differences. When the weather condition is not permitting, a minor repair can wait, without affecting the power production of the turbine. When the weather condition is permitting, the action of a minor repair is usually assumed to take place fast enough, so that the production loss it causes can be neglected. Given these understandings, how would you write the preventive maintenance cost function for a minor repair?
- 9.5 Byon [24] identifies that the mismatches between the optimal maintenance policy and the approximating maintenance policy often happen when there is a rapid transition of weather conditions from severe (a higher  $W_{PMT}$ ) to mild (a lower  $W_{PMT}$ ). Let us deem 12 m/s the wind speed limit, above which a major preventive maintenance is severely restricted.
- Use the 10-min data in the [Wind Time Series Dataset](#). Compute the probability of  $W$  as the portion of periods that wind speed is above the aforementioned limit in a week.
  - Plot  $W$  versus the weeks in a year.
  - Do you observe any time intervals where there is a noticeable transition from a severe weather condition to a mild weather condition?

# Extreme Load Analysis

---

Wind turbines operate under various loading conditions in stochastic weather environments. The increasing size and weight of components of utility-scale wind turbines escalate the loads and thus the stresses imposed on the structure. As a result, modern wind turbines are prone to experiencing structural failures. Of particular interest in a wind turbine system are the extreme events under which loads exceed a threshold, called a *nominal design load* or *extreme load*. Upon the occurrence of a load higher than the nominal design load, a wind turbine could experience catastrophic structural failures. To assess the extreme load, turbine structural responses are evaluated by conducting physical field measurements or performing aeroelastic simulation studies. In general, data obtained in either case are not sufficient to represent various loading responses under all possible weather conditions. An appropriate extrapolation is necessary to characterize the structural loads in a turbine's service life. This chapter focuses on the extreme load analysis based on physical bending moment measurements. Chapter 11 discusses load analysis based on aeroelastic simulations.

## 10.1 FORMULATION FOR EXTREME LOAD ANALYSIS

---

Fig. 10.1 presents examples of mechanical loads at different components in a turbine system. The flapwise bending moments measure the loads at the blade roots that are perpendicular to the rotor plane, whereas the edgewise bending moments measure the loads that are parallel to the plane. Shaft- and tower-bending moments measure, in two directions, respectively, the loads on the main shaft connected to the rotor and on the tower supporting the wind power generation system (i.e., blades, rotor, generator etc.).

Same as in the treatment of power response analysis, load response data are arranged in 10-minute intervals in the structural reliability analysis of wind turbines. The basic characteristics of the three inland turbines (ILT) in the Turbine Bending Moment Dataset can be found in Table 10.1. The

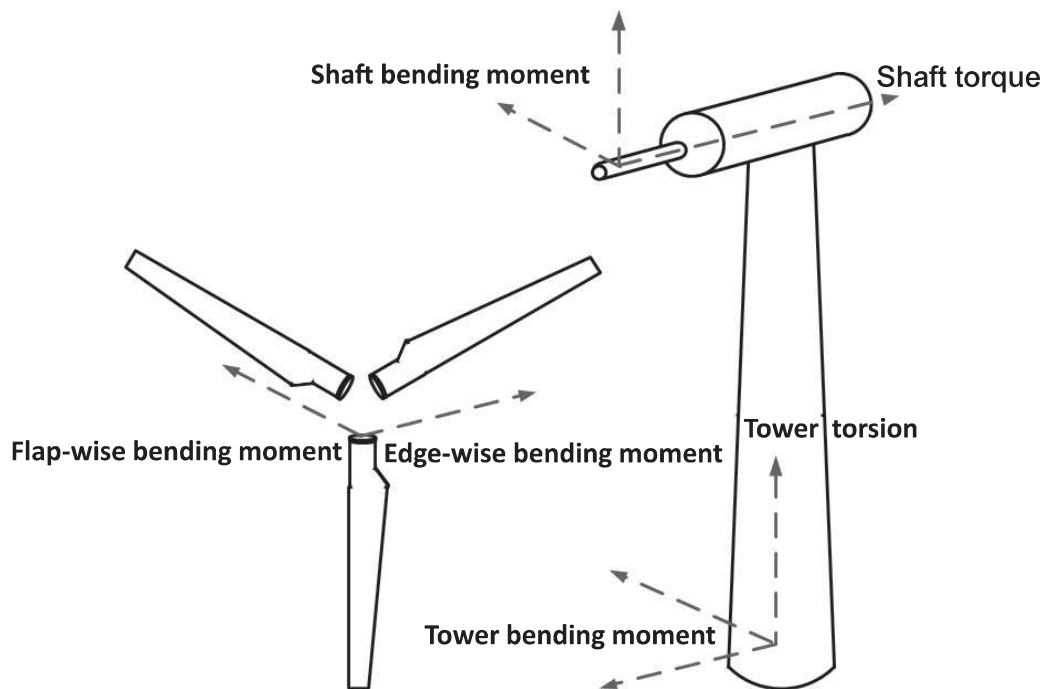


FIGURE 10.1 Illustration of structural loads at different wind turbine components. (Reprinted with permission from Lee et al. [131].)

TABLE 10.1 Specifications of wind turbines in the Turbine Bending Moment Dataset.

Turbine model (Name of dataset)	NEG-Micon/2750 (ILT1)	Vestas V39 (ILT2)	Nordtank 500 (ILT3)
Hub height (m)	80	40	35
Rotor diameter (m)	92	39	41
Cut-in speed (m/s)	4	4.5	3.5
Cut-out speed (m/s)	25	25	25
Rated speed (m/s)	14	16	12
Nominal power (kW)	2,750	500	500
Control system	Pitch	Pitch	Stall
Location	Alborg, Denmark	Tehachapi Pass, California	Roskilde, Denmark
Terrain	Coastal	Bushes	Coastal

Source: Lee et al. [131]. With permission.

original data are recorded at a much higher frequencies on the three ILTs, as follows:

- ILT1: 25 Hz = 15,000 measurements/10-min;
- ILT2: 32 Hz = 19,200 measurements/10-min;
- ILT3: 35.7 Hz = 21,420 measurements/10-min.

Consider the raw measured variables, which are wind speed,  $V_{ij}$ , and load response,  $z_{ij}$ , where  $i = 1, \dots, n$  is the index of the 10-minute data blocks and  $j = 1, \dots, m$  is the index of the measurements within a 10-minute block. The load response,  $z_{ij}$ , is the bending moment, in millions of Newton-meters, measured at designated locations. Here,  $m$  is used to represent the number of measurements in a 10-minute block, equal to 15,000, 19,200, and 21,420 for ILT1, ILT2, and ILT3, respectively, and  $n$  is used to represent the total number of the 10-minute intervals in each dataset, taking the value of 1,154, 595, and 5,688, respectively, for ILT1, ILT2, and ILT3. The statistics of the observations in each 10-minute block are calculated as

$$V_i = \frac{1}{m} \sum_{j=1}^m V_{ij}, \quad (10.1a)$$

$$s_i = \sqrt{\frac{1}{m-1} \sum_{j=1}^m (V_{ij} - V_i)^2}, \quad \text{and} \quad (10.1b)$$

$$z_i = \max \{z_{i1}, z_{i2}, \dots, z_{im}\}. \quad (10.1c)$$

After this data transformation,  $z_i$  denotes the maximum load in the  $i$ -th 10-minute block. In this study, we consider only the flapwise bending moments measured at the root of blades. In other words,  $z$  in this study is the 10-minute maximum blade-root flapwise bending moment.

Mathematically, an extreme load is defined as an extreme quantile value in a load distribution corresponding to a turbine's service time of  $T$  years [202]. Then, the load exceedance probability is defined as

$$P_T = P[z > l_T], \quad (10.2)$$

where  $P_T$  is the target probability of exceeding the load level  $l_T$  (in the same unit as that of  $z$ ). The unconditional distribution of  $z$ ,  $f(z)$ , is referred to as the *long-term* load distribution and is used to calculate  $P[z > l_T]$  in Eq. 10.2.

In Eq. 10.2, the extreme event,  $\{z > l_T\}$ , takes place with the probability of exceedance (POE),  $P_T$ . The waiting time until this event happens should be longer than, or equal to, the service time. Therefore, the exceedance probability,  $P_T$ , given the service life  $T$ , can be decided via the following way [101, 160]:

$$P_T = \frac{10}{T \times 365.25 \times 24 \times 60}. \quad (10.3)$$

Intuitively,  $P_T$  is the reciprocal of the number of 10-minute intervals in  $T$  years. For example, when  $T$  is 50,  $P_T$  becomes  $3.8 \times 10^{-7}$ .

Estimating the extreme load implies finding an extreme quantile  $l_T$  in the 10-minute maximum load distribution, given a target service period  $T$ , such that Eq. 10.2 is satisfied. Wind turbines should be designed to resist the  $l_T$  load level to avoid structural failures during its desired service life.

Since loads are highly affected by wind profiles, analysts consider the marginal distribution of  $z$  obtained by using the distribution of  $z$  conditional on a wind profile, i.e.,

$$f(z) = \int_{\mathbf{x}} f(z|\mathbf{x})f(\mathbf{x})d\mathbf{x}. \quad (10.4)$$

This expression is almost identical to that in Eq. 1.1, except that the power response,  $y$ , is replaced by the load response,  $z$ . The conditional distribution of  $z$  given  $\mathbf{x}$ ,  $f(z|\mathbf{x})$ , is referred to as the *short-term* load distribution. The long-term load distribution can be computed by integrating out wind characteristics in the short-term load distribution.

The conditional distribution modeling in Eq. 10.4 is a necessary practice in the wind industry. A turbine needs to be assessed for its ability to resist the extreme loads under the specific wind profile at the site where it is installed. Turbine manufacturers usually test a small number of representative turbines at their own testing site, producing  $f(z|\mathbf{x})$ . When a turbine is to be installed at a commercial wind farm, the wind profile at the proposed installation site can be collected and substituted into Eq. 10.4 as  $f(\mathbf{x})$ , so that the site-specific extreme load can be assessed. Without the conditional distribution model, a turbine test would have to be done for virtually every new wind farm; doing so is very costly and hence impractical.

For inland turbines, the wind characteristic vector  $\mathbf{x}$  in general comprises two elements: a steady-state mean of wind speed and the stochastic variability of wind speed [142, 183]. The first element can be measured by the average wind speed during a 10-minute interval, and the second element can be represented by the standard deviation of wind speed, or the turbulence intensity, also during a 10-minute interval. For offshore turbines, weather characteristics other than wind may be needed, such as wave height [3]. Since the data in the **Turbine Bending Moment Dataset** are all from inland turbines, what is included in  $\mathbf{x}$  in this chapter is the average wind speed  $V$  and the standard deviation of wind speed,  $s$ , namely  $\mathbf{x} := (V, s)$ .

## 10.2 GENERALIZED EXTREME VALUE DISTRIBUTIONS

The 2nd edition of the IEC 61400-1 standard, published in 1999, offers a set of design load cases with *deterministic* wind conditions such as annual average wind speeds, higher and lower turbulence intensities, and extreme wind speeds [100]. In other words, the loads in IEC 61400-1, 2nd edition, are specified as discrete events based on design experiences and empirical

models. Veers and Butterfield [223] point out that these deterministic models do not represent the stochastic nature of structural responses, and suggest instead using statistical modeling to improve design load estimates. Moriarty et al. [150] examine the effect of varying turbulence levels on the statistical behavior of a wind turbine's extreme load. They conclude that the loading on a turbine is stochastic at high turbulence levels, significantly influencing the tail of the load distribution.

In response to these developments, the 3rd edition of IEC 61400-1 standard, published in 2005 [101], replaces the deterministic load cases with *stochastic* models, and recommends the use of *statistical* approaches for determining the extreme load level in the design stage. Freudenreich and Argyriadis [67] compare the deterministic load cases in IEC61400-1, 2nd edition, with the stochastic cases in IEC61400-1, 3rd edition, and observe that when statistical approaches are applied, higher extreme load estimates are obtained in some structural responses, such as the blade tip deflection and flapwise bending moment. After the 3rd edition of IEC 61400-1 is published, several research groups devise and recommend statistical approaches for extreme load analysis [3, 65, 67, 149, 153, 174].

According to the classical extreme value theory [38, 200], the short-term distribution,  $f(z|\boldsymbol{x})$ , can be approximated by a generalized extreme value (GEV) distribution. The pdf of the GEV is

$$f(z) = \begin{cases} \frac{1}{\sigma} \exp \left[ - \left( 1 + \xi \left( \frac{z-\mu}{\sigma} \right) \right)^{-\frac{1}{\xi}} \right] \left( 1 + \xi \left( \frac{z-\mu}{\sigma} \right) \right)^{-1-\frac{1}{\xi}}, & \xi \neq 0, \\ \frac{1}{\sigma} \exp \left[ - \frac{z-\mu}{\sigma} - \exp \left( - \frac{z-\mu}{\sigma} \right) \right], & \xi = 0, \end{cases} \quad (10.5)$$

for  $\{z : 1 + \xi(z - \mu)/\sigma > 0\}$ , where  $\mu$  is the location parameter,  $\sigma > 0$  is the scale parameter, and  $\xi$  is the shape parameter that determines the weight of the tail of the distribution. When  $\xi > 0$ , the GEV corresponds to the Fréchet distribution family with a heavy upper tail,  $\xi < 0$  to the Weibull distribution family with a short upper tail and light lower tail, and  $\xi = 0$  (or,  $\xi \rightarrow 0$ ) to the Gumbel distribution family with a light upper tail.

The cdf of the GEV distribution is

$$F(z) = \begin{cases} \exp \left[ - \left( 1 + \xi \left( \frac{z-\mu}{\sigma} \right) \right)^{-\frac{1}{\xi}} \right], & \xi \neq 0, \\ \exp \left[ - \exp \left( - \frac{z-\mu}{\sigma} \right) \right], & \xi = 0. \end{cases} \quad (10.6)$$

Recall the cdf of Weibull distribution in Eq. 2.5. If modified to be a three-parameter Weibull distribution with a location parameter  $\mu$ , the cdf reads

$$F(z) = 1 - \exp \left[ - \left( \frac{z-\mu}{\eta} \right)^\beta \right].$$

Although one can discern that  $\beta$  here is related to  $\xi$  in the GEV distribution and  $\eta$  to  $\sigma$ , the two distributions do not appear the same for  $\xi \neq 0$ . One may wonder why when  $\xi < 0$ , the GEV distribution is said to be corresponding

to the Weibull distribution family. The reason behind the disconnect is that the GEV distribution of  $\xi < 0$  corresponds actually to the reverse Weibull distribution, which is the negative of the ordinary Weibull distribution. Recall that a Weibull distribution is used to describe a non-negative random variable with a right-side skewness, like wind speed. The ordinary Weibull distribution deals with the minimum and has a lower bound. The GEV distribution when  $\xi < 0$  deals instead with the maximum and sets an upper bound, so that the distribution looks like the mirror image of the ordinary Weibull distribution. The cdf of a reserve Weibull is

$$F(z') = \begin{cases} \exp[-(-z')^\beta], & z' < 0, \\ 1, & z' \geq 0. \end{cases} \quad (10.7)$$

If we let  $\beta = -1/\xi$  and  $z' = -(1 + \xi(z - \mu)/\sigma)$ , then one sees that the cdf expression in Eq. 10.6 for  $\xi < 0$  and that in Eq. 10.7 are the same.

One of the main focuses of interest in the extreme value theory is to derive the quantile value, given a target probability  $P_T$ . The extreme quantile value based on a GEV distribution of  $z$  is in fact the design load threshold,  $l_T$ , in Eq. 10.2. Given a  $P_T$ ,  $l_T$  can be expressed as a function of the distribution parameters as

$$l_T = \begin{cases} \mu - \frac{\sigma}{\xi} \left[ 1 - (-\log(1 - P_T))^{-\xi} \right], & \xi \neq 0, \\ \mu - \sigma \log[-\log(1 - P_T)], & \xi = 0. \end{cases} \quad (10.8)$$

### 10.3 BINNING METHOD FOR NONSTATIONARY GEV DISTRIBUTION

---

When using a GEV distribution to model  $z$ , one difficulty is that  $z$  appears to be a function of input  $\mathbf{x}$ . Using the three datasets, Lee et al. [131] present a number of scatter plots to illustrate this point. Fig. 10.2 shows the scatter plots between the 10-minute maximum loads and 10-minute average wind speeds. One observes nonlinear patterns between the load and the average wind speed in all three scatter plots, while individual turbines exhibit different response patterns. ILT1 and ILT2 are two pitch-controlled turbines, so when the wind speed reaches or exceeds the rated wind speed, the blades are adjusted to reduce the absorption of wind energy. As a result, the load shows a downward trend after the rated speed. Different from that of ILT1, the load response of ILT2 has a large variation beyond the rated wind speed. This large variation can be attributed to its less capable control system since ILT2 is one of the early turbine models using a pitch control system. ILT3 is a stall controlled turbine, and its load pattern in Fig. 10.2(c) does not have an obvious downward trend beyond the rated speed.

Fig. 10.3 presents the scatter plots between the 10-minute maximum loads and the standard deviations of wind speed during the 10-minute intervals. One

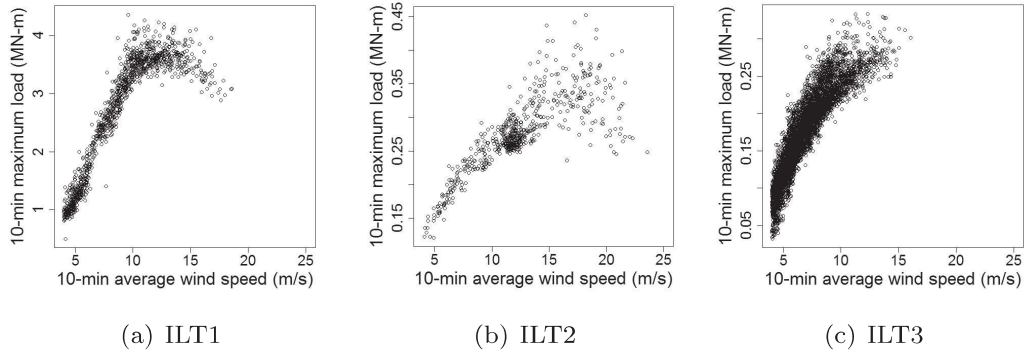


FIGURE 10.2 Scatter plots of 10-minute maximum load versus 10-minute average wind speed. (Reprinted with permission from Lee et al. [131].)

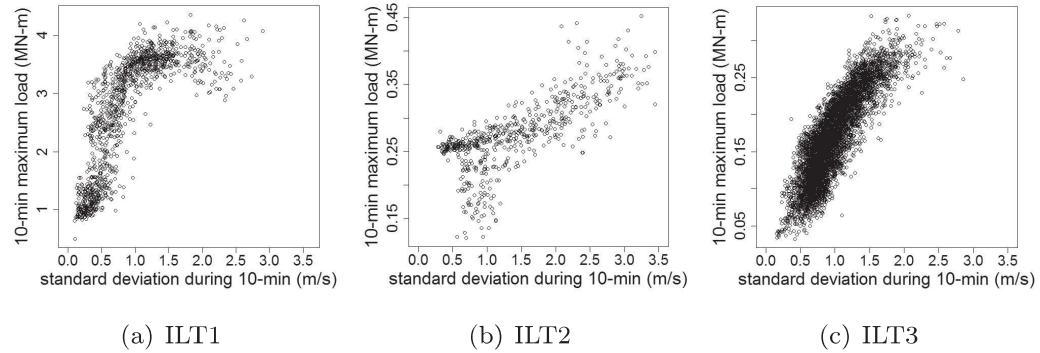


FIGURE 10.3 Scatter plots of 10-minute maximum load versus 10-minute standard deviations of wind speed. (Reprinted with permission from Lee et al. [131].)

also observes nonlinear relationships between them, especially for the newer pitch-controlled ILT1.

Fig. 10.4 shows scatter plots of 10-minute standard deviation versus 10-minute average wind speed. Previous studies [63, 150] suggest that the standard deviation of wind speed varies with the average wind speed, which appears consistent with what is observed in Fig. 10.4.

This type of load response, varying with the input conditions, is known as inhomogeneous or nonstationary response. If a set of constant parameters,  $\{\mu, \sigma, \xi\}$ , is used in modeling a GEV distribution, the resulting distribution is homogenous or stationary for the entire input domain, which does not match the inhomogeneous reality of the turbine load condition. To address this issue, analysts in the aforementioned extreme load analysis adopt a common framework, referred to as the *binning* approach [131]. The basic idea of the binning method is the same as that used for power curve analysis in Chapter 5, but

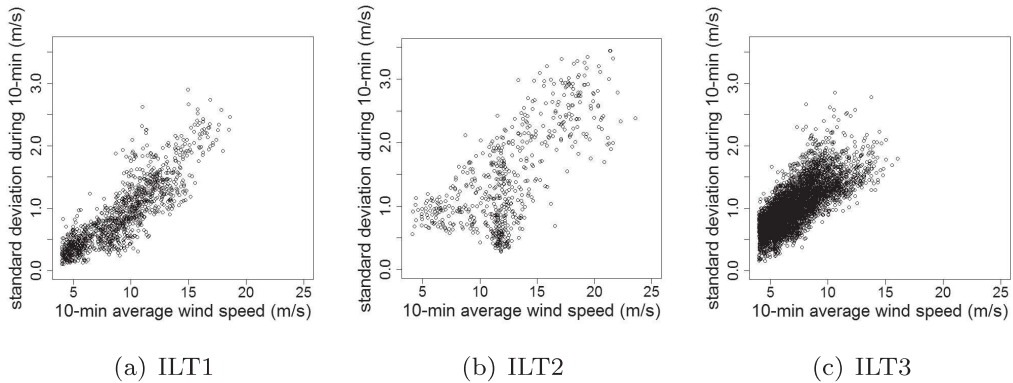


FIGURE 10.4 Scatter plots of 10-minute average wind speed versus 10-minute standard deviations of wind speed. (Reprinted with permission from Lee et al. [131].)

unlike power curve analysis in which a simple sample average is used to model the data in a bin, a GEV distribution is established in each bin in extreme load analysis.

Specifically, the binning approach discretizes the domain of a wind profile vector  $\mathbf{x}$  into a finite number of bins. One can divide the range of wind speed, from the cut-in speed to the cut-out speed, into multiple bins and set the width of each bin to, say, 2 m/s. Then, in each bin, the conditional short-term distribution,  $f(z|\mathbf{x})$ , is approximated by a stationary GEV distribution, with the parameters of the distribution fixed at certain constants and estimated by the maximum likelihood method, using the data specific to that bin. The contribution from each bin is summed over all possible bins to determine the final long-term extreme load. In other words, the integration in Eq. 10.4 for calculating the long-term distribution is approximated by the summation of finite elements. The idea of binning is illustrated in Fig. 10.5.

The virtue of the binning method is that by modeling the short-term distribution with a homogeneous GEV distribution, i.e., keeping the GEV distribution parameters constant for a given bin, it provides a simple way to handle the overall nonstationary, inhomogeneous load response across different wind covariates. Assuming the load response stationary or homogenous in a narrow range within a wind speed bin is much more reasonable than assuming stationarity or homogeneity for the entire wind spectrum.

The common binning approach, as Agarwal and Manuel [3] use it to estimate the extreme loads for a 2MW offshore wind turbine, is to use the Gumbel distribution to model the probabilistic behavior of bending moments at critical spots on a turbine structure. To estimate the model parameters, experimental data are collected but only for a short period, say one or two years. As a result, most bins have a small number of data, or sometimes, no data at all. For the bins without data, Agarwal and Manuel estimate the short-term distribution parameters by using a weighted average of all non-empty bins with the weight

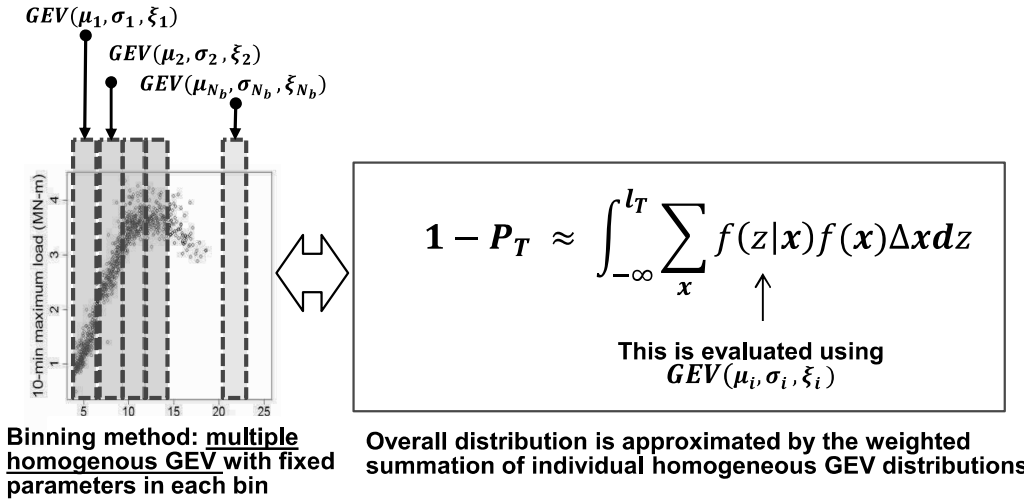


FIGURE 10.5 Binning approach to combine bin-based homogenous GEV distributions for extreme load analysis over the entire wind spectrum. In implementation,  $\xi_i$ ,  $i = 1, \dots, N_b$ , is chosen to be the same constant for all bins.

related to the inverse squared distance between bins. They quantify the uncertainty of the estimated extreme loads using bootstrapping and report the 95% confidence interval for the short-term extreme load given specific weather conditions (i.e., weather bins). Because bootstrapping resamples the existing data for a given weather bin, it cannot precisely capture the uncertainty for those bins with limited data or without data.

Lee et al. [131] present explicit steps to calculate the confidence interval for the binning method. First, they fix  $\xi$  to be a constant across all bins. The typical choice of  $\xi$  is zero, meaning that a Gumbel distribution is used. But  $\xi$  can also be estimated *a priori* and then remains fixed while other parameters are being estimated. After  $\xi$  is fixed, the resulting GEV distribution has then two bin-specific parameters,  $\mu$  and  $\sigma$ . Denote by  $\Phi_c$  the collection of parameters associated with all local GEV distributions, i.e.,  $\{\mu_1, \sigma_1, \dots, \mu_{N_b}, \sigma_{N_b}, \xi\}$ , where  $N_b$  is the number of bins, and by  $\mathcal{D}_V$  and  $\mathcal{D}_s$  the datasets of the observed average wind speeds and the standard deviations. The sampling process is elaborated in Algorithm 10.1.

Despite its popularity, the binning method has obvious shortcomings in estimating extreme loads. A major limitation is that the short-term load distribution in one bin is constructed separately from the short-term distributions in other bins. This approach requires an enormous amount of data to define the tail of each short-term distribution. In reality, the field data can only be collected in a short duration (e.g., one year out of 50 years of service), and consequently, some bins do not have enough data. Then, the binning method may end up with inaccuracy or high uncertainty in the estimates of extreme